

Fluid–rock interactions related to metamorphic reducing fluid flow in meta-sediments: example of the Pic-de-Port-Vieux thrust (Pyrenees, Spain)

Vincent Trincal^{1,2} · Martine Buatier¹ · Delphine Charpentier¹ · Brice Lacroix³ · Pierre Lanari⁴ · Pierre Labaume⁵ · Abdeltif Lahfid⁶ · Torsten Vennemann⁷

Received: 7 December 2016 / Accepted: 18 July 2017 / Published online: 18 August 2017
© Springer-Verlag GmbH Germany 2017

Abstract In orogens, shortening is mainly accommodated by thrusts, which constitute preferential zones for fluid–rock interactions. Fluid flow, mass transfer, and mineralogical reactions taking place along thrusts have been intensely investigated, especially in sedimentary basins for petroleum and uranium research. This study combines petrological investigations, mineralogical quantifications, and geochemical characterizations with a wide range of analytical tools with the aim of defining the fluid properties (nature, origin, temperature, and redox) and fluid–host rock interactions (mass transfers, recrystallization mechanisms,

and newly formed synkinematic mineralization) in the Pic-de-Port-Vieux thrust fault zone (Pyrenees, Spain). We demonstrate that two geochemically contrasted rocks have been transformed by fluid flow under low-grade metamorphism conditions during thrusting. The hanging-wall Triassic red pelite was locally bleached, while the footwall Cretaceous dolomitic limestone was mylonitized. The results suggest that thrusting was accompanied by a dynamic calcite recrystallization in the dolomitic limestone as well as by leaching of iron via destabilization of iron oxides and phyllosilicate crystallization in the pelite. Geochemical and physical changes highlighted in this study have strong implications on the understanding of the thrust behavior (tectonic and hydraulic), and improve our knowledge of fluid–rock interactions in open fluid systems in the crust.

Communicated by Franck Poitrasson.

Electronic supplementary material The online version of this article (doi:[10.1007/s00410-017-1394-5](https://doi.org/10.1007/s00410-017-1394-5)) contains supplementary material, which is available to authorized users.

✉ Vincent Trincal
vincenttrincal@gmail.com

¹ UMR Chrono-Environnement, Université de Bourgogne Franche-Comté, 16 Route de Gray, 25030 Besançon, France

² Département GCE, Ecole des Mines, IMT Lille Douai, University of Lille, 764, Boulevard Lahure, 59508 Douai, France

³ Department of Geology, Kansas State University, 108 Thompson Hall, Manhattan, KS 66506, USA

⁴ Institute of Geological Sciences, University of Bern, Baltzstrasse 1+3, 3012 Bern, Switzerland

⁵ Géosciences Montpellier, UMR 5243, Université de Montpellier-CNRS, 34095 Montpellier, France

⁶ BRGM, 3 Avenue Claude Guillemin, BP 36009, 45060 Orléans Cedex 2, France

⁷ Institut des Sciences de la Terre (ISTE), Université de Lausanne, 1015 Lausanne, Switzerland

Keywords Fluid–rock interaction · Mass transfer · Pelite discoloration · Mylonitization · Mössbauer spectroscopy · Stable isotope

Introduction

In fold-and-thrust belts, shortening is mainly accommodated by thrust faults which are preferential zones for fluid flow and related mass transfers. Fault zone behavior with respect to fluids is influenced by many mineralogical and mechanical reactions (e.g., Caine et al. 1996; Faulkner et al. 2010). For example, due to fluid–rock interactions, a single fault zone can evolve from a preferential fluid pathway to a barrier. Due to their economic importance in oil and gas industries, physical properties of fault zones during basin deformation evolution were widely studied during the last decades, especially their porosity and permeability (e.g., Zhang and Tullis 1998; Fisher and Knipe 2001; Zhang et al.

2011). However, to fully understand the mechanisms related to the fluid–rock interactions in fault zones, it is necessary to investigate the role of host rock properties such as their mineralogy and chemical composition, as well as that of ambient pressure and temperature conditions during fault activity. Furthermore, physical and chemical fluid characteristics must also be investigated, including their nature and origin, temperature and pressure (which could be different from that of the host rock), chemical composition, redox/ fO_2 , and X_{CO_2} . A large number of studies relevant to the role of physical and chemical parameters and mechanisms involved during thrusting were recently produced (see, for instance, Lacombe et al. 2014), but most of these studies remain focused on a few specific aspects of the problem. Many questions remain unsolved, especially regarding the coupling between deformation and mass transfer in fault zones crossing sedimentary rocks under greenschist facies conditions.

This study focuses on the Pic-de-Port-Vieux (PPV) thrust in the southern part of the Pyrenean Axial Zone (Fig. 1), because it was previously well described by several stratigraphic, structural, fluid flow, and pressure–temperature studies (e.g., Parish 1984; Grant 1989, 1990, 1992; McCaig et al. 1995, 2000a, b, c). The PPV thrust separates Triassic

red pelites in the hanging-wall from Cretaceous marine carbonates in the footwall. Recent works demonstrated that the PPV thrust was open to metamorphic fluid flow, resulting in the formation of metamorphic minerals under greenschist facies conditions (Lacroix et al. 2014; Trincal et al. 2015; Abd Elmola et al. 2017). The study of the PPV thrust thus provides the opportunity to investigate the interaction between a metamorphic fluid and two distinct sedimentary layers with different geochemical and physical properties. The physical and chemical parameters of the system were investigated using a large range of analytical methods (petrographic observations and XRD mineral quantifications, stable isotope geochemistry, Raman and Mössbauer spectroscopies, and geothermometry). The mineralogical reactions and mass transfers induced by fluid flow in both host rocks were assessed and a fluid–rock interaction model during thrusting was produced.

Geological settings and sampling

The Pyrenean belt is a double-vergence orogenic wedge formed during the Late Cretaceous to the early Miocene by the collision of the Iberian and European plates (e.g., Muñoz

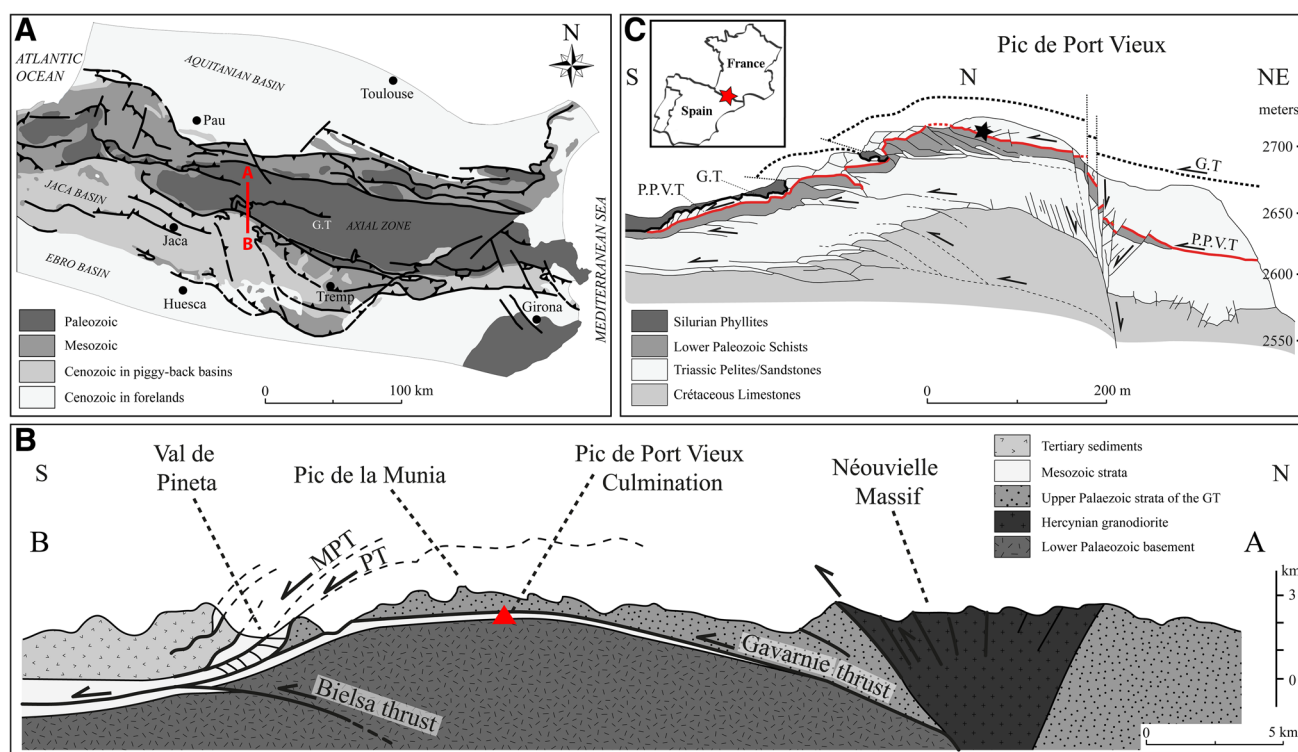


Fig. 1 **a** Structural map of the Pyrenees with location of the cross section in **b** (modified from Teixell 2000). **b** Cross-sectional AB through the Gavarnie thrust sheet showing the location of the study area (Pic-de-Port-Vieux) modified from Grant (1992) and Jolivet et al.

(2007). **c** Sketch of the Pic-de-Port-Vieux culmination, modified from Grant (1989). Key: G.T: Gavarnie thrust, MPT: Monte Perdido thrust; P.P.V.T: Pic-de-Port-Vieux thrust, PT: Pineta thrust

1992; Roure et al. 1989; Teixell 1998). The south-vergent thrust system comprises imbricated basement thrusts, which form the anticlinal stack of the Axial Zone and pass southwards to detachment levels below the cover thrust units of the South-Pyrenean Zone. The PPV thrust is a minor thrust located in the south-western part of the Pyrenean Axial Zone, in the footwall of the major Gavarnie thrust (Fig. 1). The PPV thrust affects both basement rock and their sedimentary cover. The basement rocks consist of migmatized psammites and schists locally intruded by Hercynian granodiorites (Grant 1990). The basement was affected by greenschist facies metamorphism (with the development of pyrophyllite and phengite) during the Pyrenean orogeny (Grant 1989). Above, the sedimentary cover consists of Triassic continental red sandstones and pelites followed by Upper Cretaceous marine dolomitic limestones. In the studied area, the PPV thrust superposes Triassic redbeds onto Cretaceous carbonates with a minimum displacement

of 0.85 km (Grant 1990). The hanging-wall redbeds are themselves overthrust by the Gavarnie thrust. The Gavarnie thrust hanging-wall comprises a basal décollement layer of Silurian phyllites followed by Devonian–Carboniferous carbonates and flysch, with a minimum displacement of 11.5 km (e.g., Parish 1984; Soler et al. 1998). The duration of Gavarnie thrust activity is estimated at 4.3 million years (Labaume et al. 2016).

Both Gavarnie and PPV thrusting occurred at a fluid pressure of 1.5–2 kbar, corresponding to 5–7.5 km burial depth under lithostatic conditions (Grant 1990). The propagation of PPV thrust folded the overlying Gavarnie thrust, showing that the PPV thrust is younger than to the Gavarnie thrust. However, this does not exclude the possibility that both thrusts were contemporaneously. Structures and microstructures in the PPV fault zone were extensively described by Grant (1989, 1992) and Trincal et al. (2015) (Fig. 2a, b). The core zone corresponds to an up to 2 m-thick layer of

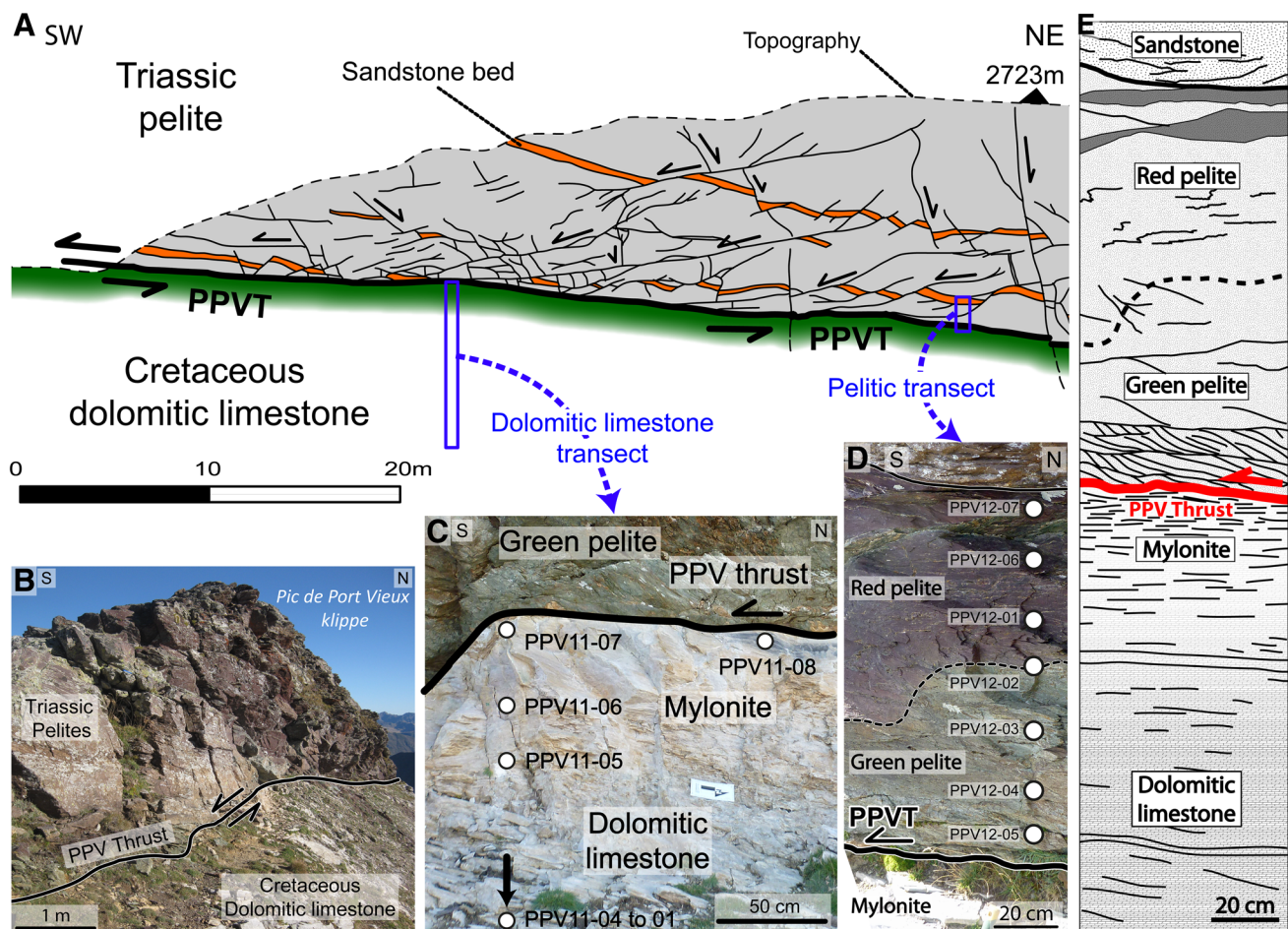


Fig. 2 **a** Pic-de-Port-Vieux outcrop cross section modified from Grant (1989) with location of the studied profiles (PPVT: Pic-de-Port-Vieux thrust surface). The hanging-wall is composed by Triassic pelitic rocks intercalated with sandstone beds; it is deformed by a complex array of secondary faults and veins; the footwall comprises

Upper Cretaceous dolomitic limestone mylonitized against the thrust surface. **b** View of the Pic-de-Port-Vieux outcrop. **c** Limestone-to-calc-mylonite profile and sample location in the PPVT footwall. **d** Pelitic profile and sampling location in the PPVT hanging-wall. **e** Representative log across the PPVT

mylonitized dolomitic limestone in the footwall and a few cm-thick shear zone in the hanging-wall pelites. Above the basal shear zone, the hanging-wall comprises a 10 m-thick damage zone with cleavage, secondary faults, fractures, and veins. Grant (1992) described six deformation stages in the PPV thrust fault zone. According to Grant (1990, 1992), Banks et al. (1991) and McCaig et al. (2000c) and based on structural data, the PPV footwall dolomitic limestone mylonitization started during the Gavarnie thrusting and continued during the PPV thrusting. Mylonites have highly variable permeability, but generally higher than the undeformed dolomitic limestone. Mylonite can, therefore, allow important fluid flow in the direction parallel to mylonitic foliation (Knipe and McCaig 1994; McCaig et al. 1995). Therefore, fluid flow in the thrust probably generated both mineralogical transformations in the footwall calc-mylonites and synkinematic veins in the hanging-wall pelites, especially during reactivation episodes (by spreading/gliding during post-emplacement stage in Grant 1992).

Sampling was conducted in the summit klippe of the Pic-de-Port-Vieux culmination to study the mineralogical transformations and the mass transfers induced in host rocks by fluid flow along the thrust zone. Host rock samples were collected along 2 m-long profiles on both sides of the thrust surface, avoiding veins where possible. The footwall profile comprises dolomitic limestone (i.e., partially dolomitized limestone during diagenesis) that becomes progressively mylonitized close to the thrust (Fig. 2c, e). The hanging-wall profile consists of red pelites, whose color turns to greenish close to the main thrust surface and around secondary faults (Fig. 2d, e). This study focuses exclusively on pelitic rocks, which is the main lithology of the hanging-wall. In addition to carbonate and pelitic host rocks, two quartz–chlorite veins were sampled for isotopic analyses in the hanging-wall to performed temperature estimations. The sampled veins were selected in the field assuming their contemporaneity with the formation of the limestone mylonites and also with discoloration of pelites. The footwall mylonites could have easily been reactivated or inherited from the Gavarnie thrust movement, as discussed by various authors (e.g., Grant 1989).

Methodology

Petrographic and mineralogical characterization

Petrographic observations were made with a JEOL JSM5600 scanning electron microscope (SEM) coupled with a FONDIS energy dispersive analyser (EDS) in the Renatech network FEMTO-ST laboratory and with an optical microscope coupled with cathodo-luminescence (CL) using a cold cathode equipment operating at 18.5 ± 1.5 keV and

250 ± 50 mA, both at the University of Franche-Comté (Besançon).

Samples were ground either by hand in an agate mortar or with a mechanical crusher for bulk XRD analyses. No significant differences in the results were observed between the two grinding techniques. XRD analyses were performed on selected powders at the University of Franche-Comté using a Bruker D8 Advance diffractometer system using Cu–K α radiation equipped with a fast LynxEye linear detector. The diffractometer was operated at 40 kV and 40 mA. Scans were run from 5° to $120^\circ 2\theta$, with a step interval of $0.02^\circ 2\theta$ and a goniometry speed of 1 s per step.

The identification of the mineral phases was performed using the Bruker-AXS's DiffracPlus EVA software and the ICDD Powder Diffraction File 2008 database (The International Centre for Diffraction Data). Mineral quantification was made by Rietveld refinement (Rietveld 1969) using the fundamental parameters approach (Cheary and Coelho 1992) of the DIFFRACplus TOPAS software, version 4.2 (2009, Bruker AXS). The Rietveld method consists in minimizing the difference between a diffractogram calculated for a given starting model and the experimental diffractogram. Crystal structure data for calcite, chlorite, dolomite, hematite, muscovite, and quartz were taken from the ICDD PDF and Bruker Structure Database. The polytypes of the two phyllosilicates were selected according to characteristic peaks (Moore and Reynolds 1997) and the site occupancies of their structures were adjusted using electron microprobe analyses. Rietveld refined parameters used, such as unit cell parameters, isotropic temperature factors, weight fractions of the phase present, coherent single scattering domain sizes, and preferred orientation parameters (March Dollase model), are described in detail in Trincal et al. (2014). Mineral content standard deviations were obtained by the multiplication of the GOF (goodness of fit) by the standard deviation given by the Topas software to have a real approximation (Taylor and Hinczak 2003; Trincal et al. 2014).

Geochemical analyses

The mineral chemical compositions were determined on carbon coated thin sections using a CAMECA model SX100 electron microprobe equipped with five wave dispersive spectrometers at the University of Montpellier. The microprobe was operated at 20 keV, with a beam current of 10 nA and a beam diameter of 3 μ m. The standards used for phyllosilicate analyses were albite (Na), Al_2O_3 (Al), Fe_2O_3 (Fe), forsterite (Mg), orthoclase (K), TiO_2 (Ti), and wollastonite (Si, Ca) (for the choice of standards see Merlet and Bodinier 1990). To obtain reliable data and to avoid contamination by edge effects, only grains larger than 10–20 μ m were analyzed. Microprobe analyses were used for Rietveld refinement and normative estimation, especially for white mica

and chlorite that can have a wide range of chemical compositions (e.g., Cathelineau 1988).

Major element analyses were carried out by X-ray Fluorescence Spectrometry (XRF) at the Centre d'Analyse Minérale (CAM), University of Lausanne. Bulk rock analyses were performed using a Philips PW2400 spectrometer equipped with a rhodium anode. Measurements were performed on melted tablets 4 cm in diameter, requiring 10–15 g of powdered rock. The detection limit is approximately 0.01%.

O- and C-isotope compositions of carbonate samples, comprising both calcite and dolomite, were obtained by drilling out approximately 5 mg of powder with a diamond bit. The isotopic compositions ($\delta^{18}\text{O}$ and $\delta^{13}\text{C}$) were determined following the method of Spötl and Vennemann (2003). CO_2 was produced from ~250 μg of carbonate powder reacting with hydrochloric acid at 90 °C for 1 h. The produced CO_2 was removed with a helium stream and analyzed using a Gas-Bench on a Finnigan MAT DeltaPlus XL mass spectrometer at the University of Lausanne. The oxygen- and carbon-isotope compositions are reported in the delta notation (δ), expressed relative to SMOW in permil (‰). The results were corrected using the international standard NBS-19. The analytical uncertainty was lower than 0.05‰ for $\delta^{13}\text{C}$ and 0.1‰ for $\delta^{18}\text{O}$.

Chlorite and quartz grains were hand-picked from crushed vein samples and then washed in distilled water and ethanol to remove fine powder and reduce the static magnetic effect. Quartz–chlorite pairs were analyzed for oxygen isotope compositions at the stable isotope laboratory of University of Lausanne using a CO_2 -laser fluorination line coupled with a Finnigan MAT 253 mass spectrometer, following a method similar to those described by Sharp (2009), Rumble and Hoering (1994) and Kasemann et al. (2001). Oxygen isotope compositions are given in the standard δ -notation, expressed relative to SMOW in permil (‰). The accuracy of $\delta^{18}\text{O}$ values is in the range of precision of the LS-1 quartz standards used with a $\delta^{18}\text{O}$ value of 18.1 ± 0.1 ‰.

Measurements of hydrogen isotope compositions of vein chlorite were performed at the University of Lausanne using high-temperature (1450 °C) reduction methods with H_2 carrier gas and a TC-EA linked to a Delta Plus XL mass spectrometer from Thermo–Finnigan. The results are given in the standard δ -notation, expressed relatively to SMOW in permil (‰). The precision for hydrogen isotope analyses is better than ± 2 ‰ and was estimated using the standards kaolinite and G1 biotite of the University of Lausanne.

Mössbauer data were carried out on pelitic samples at the LCPME laboratory in Nancy, France. Mössbauer spectra were accumulated at RT, with a constant-acceleration spectrometer and a 512 multichannel analyser, manufactured by Halder Elektronik GmbH, and a 50 mCi source of ^{57}Co in Rh matrix maintained at room temperature. The folding was

performed to achieve a flat background. The velocity was calibrated with a 25 lm foil of a-Fe at room temperature and the isomer shifts are given with respect to this reference. The samples were set in the sample holder and introduced in the cryostat (Advanced Research Systems). The amount of materials being optimized were 10 mg of Fe/cm^2 , and the spectra were fit with the lorentzian-shape line model fitting method of Rancourt and Ping (1991) for quadrupole splitting distributions. The measurements were performed with a velocity range of ± 11 mm/s or in an expanded velocity range of ± 4 . The larger range allowed possible detection of magnetically split patterns from Fe oxides, while the smaller range gave an optimal resolution for the sample. Hematite, composed only of Fe^{3+} , is easily identifiable by its characteristic hyperfine parameters: isomer shift (CS) = 0.4 mm/s, quadrupole splitting (QS) = -0.1 , and hyperfine field $H = 512$ to 515 kOe. For phyllosilicates, the Fe^{3+} content can be easily distinguished from Fe^{2+} with QS and CS hyperfine parameters (e.g., Bowen et al. 1969; Heller-Kallai and Rozenson 1981). CS values between 0.3 and 0.6 mm/s are attributed to Fe^{3+} , while values between 1.0 and 1.2 mm/s are attributed to Fe^{2+} ions. However, chlorite and muscovite have very similar hyperfine parameters (e.g., Bowen et al. 1969; Coey 1980; Heller-Kallai and Rozenson 1981; Kodama et al. 1982; De Grave et al. 1987; Aja and Dyar 2002). The similarity of the phyllosilicate hyperfine parameters does not permit the assignment of Fe^{3+} and Fe^{2+} to mica or chlorite. For example, a CS value of 1.1 mm/s coupled with a QS value of 2.6 mm/s can be attributed to a part of Fe^{2+} content of muscovite or chlorite indifferently.

Geothermometry

The degree of organization of the carbonaceous material in meta-sediments can be quantified by Raman Spectroscopy of Carbonaceous Material (RSCM) and used to derive the maximum temperature of metamorphism (Pasteris and Wopenka 1991; Ferrari and Robertson 2000; Beyssac et al. 2002; Lahfid et al. 2010; Aoya et al. 2010). RSCM thermometer was first calibrated in the range 330–640 °C (Beyssac et al. 2002) then extended to 200–350 °C, both calibrations having a relative accuracy of ± 25 °C (Lahfid et al. 2010). Raman measurements were performed on footwall samples (in both dolomitic limestone and calc-mylonite) with a Renishaw InVIA Reflex microspectrometer coupled with a DMLM 2500 Leica microscope and an argon excitation laser of 514.5 nm. The samples were analyzed using uncovered polished thin sections. The Raman spectrometer was operated using continuous scanning mode with spectral windows from 700 to 2000 cm^{-1} . Calibration was performed using the 520.4 cm^{-1} line of silicon.

Chlorite thermometry was used to assess the temperature of chlorite formation. This thermometer is based on

three main chemical substitutions in chlorite: Tschermak, Fe–Mg, and di-trioctahedral one (e.g., Lanari et al. 2014 and references therein). In addition, the chlorite redox conditions ($\text{Fe}^{3+}/\text{Fe}_{\text{Tot}}$) must be taken into account for the temperature calculation (Trincal and Lanari 2016; Vidal et al. 2016). If XANES or Mössbauer XFe^{3+} data are not available for the analyzed chlorite, as it is the case in this study, it is better to use the Vidal et al. (2005, 2006) approach that allows temperature and XFe^{3+} estimation based on the convergence of four (two independent) equilibria involving five chlorite end-members, quartz, and a pure H_2O fluid. XFe^{3+} of chlorite predicted by this technique satisfactorily reproduces the speciation measurements (Vidal et al. 2016). Formation temperatures of chlorite were calculated from oxide wt% using the program CHLMICA-EQUI 1.5 (Lanari 2012; Lanari et al. 2012). The temperature and XFe^{3+} (within the range of 0.05–0.5) of chlorite were estimated at a reference pressure of 5 kbar and a fixed $a_{\text{H}_2\text{O}}$ of 1. The absolute uncertainty on the formation temperature is 50 °C (Vidal et al. 2005, 2006), whereas the relative uncertainty is generally comprised between 7 and 20 °C (Cantarero et al. 2014).

The formation temperature of the veins related to the PPV thrusting is constrained by oxygen isotope fractionation between cogenetic quartz and chlorite using the fractionation model proposed by Lacroix and Vennemann (2015). This empirical calibration is based on natural chlorite samples presenting XFe between 0.4 and 0.7, and is, therefore, appropriate for the chlorite compositions studied here.

Results

Carbonate footwall characterization

The footwall dolomitic limestone is mylonitized up to 2 m from the thrust surface. Heterogeneities appear at the outcrop scale, with calcite-rich and dolomite-rich layers following the bedding-parallel foliation (Fig. 3a). The dolomite-rich layers could represent less than 2 vol% (Banks et al. 1991) and display conjugate veins suggesting a brittle behavior. By contrast, the calcite-rich layers are devoid of veins, probably due to a more ductile deformation, or these veins were mylonitized (Knipe and McCaig 1994). Calc-mylonite

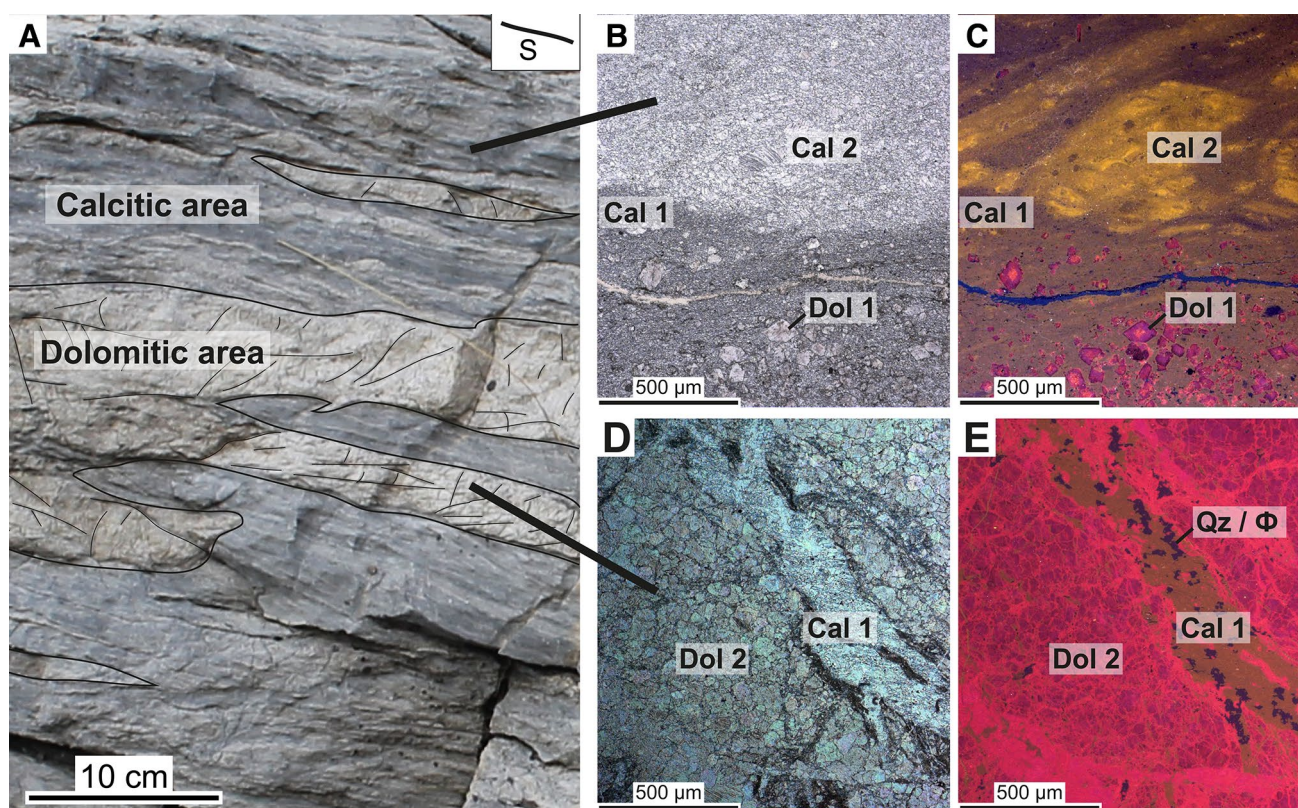


Fig. 3 Dolomitic limestone in the PPV thrust footwall. **a** Outcrop view showing fractured dolomitic layers and calcitic layers. S: bedding-parallel foliation. Plain light (**b**) and cathodo-luminescence (**c**) microscope images of calcite-rich domain showing two calcite generations (Cal1 and Cal2) and dolomitic euhedral crystal (Dol1).

Plain light (**d**) and cathodo-luminescence (**e**) microscope images of dolomite-rich domain showing fractured dolomite (Dol2) and slightly recrystallized calcite matrix associated with quartz and porosity (Qz/ϕ)

has a lighter color (Fig. 2c) and shows a fine and homogeneous mineralogy suggested by a subconchoidal fracture at the sample scale. Both lithologies are mainly composed by calcite, dolomite, and quartz. Based on XRD analyses (Appendix 1), Rietveld refinement quantifications (verified by normative calculations) suggest that calcite ranges between 86 and 97 wt% and dolomite between 2 and 9 wt%, except for one sample which contains 73 wt% of dolomite and 25 wt% of calcite (Table 1; Fig. 4). These analyses likely reflect the mineralogical heterogeneity between calcite-rich and dolomite-rich layers previously observed. Calc-mylonite samples located immediately below the thrust fault have the lowest dolomite content. Quartz is present in small quantities (<5 wt%) in footwall samples and is probably related to the occurrence of siliceous fossils or to small veins. Rare phosphates (apatite) and iron oxide minerals (framboidal pyrite and ankerite) are locally observed with SEM, but are not detected by XRD, supporting their scarcity (<1 wt%). Pyrite can be surrounded or partially replaced by ankerite (Fig. 5a) suggesting an early diagenetic origin preserved from further re-equilibration during burial diagenesis or low-grade metamorphism (ref. in Charpentier et al. 2011).

The dolomitic limestone shows several carbonate generations (Fig. 3). In calcite-rich layers, calcite occurs as brown micrite (Cal1) associated with fossils and dispersed small quartz, or as yellow microsparite (Cal2) visible in CL; dolomite (Dol1) occurs as purple in CL euhedral zoned crystals dispersed in micrite (Fig. 3b, c). In dolomite-rich layers, dolosparite (Dol2) occurs as an accumulation of cleaved xenomorphic grains around a domain composed of micritic calcite (Cal1), which seems slightly recrystallized and enriched in small quartz (Fig. 3d, e). In calc-mylonite (Fig. 6a), anhedral dolomite crystals (Dol2) are partially replaced by newly formed micritic calcite (Cal3) occurring as yellow in CL. The evidence of local dolomite dissolution

associated with newly formed calcite crystallization can be observed by SEM (Fig. 5b). Finally, micrite–microsparite (Cal4) is greenish in CL and occurs in both matrix and veins (Fig. 6b, c).

Oxygen- and carbon-isotope compositions of samples from the footwall profile are reported in Figs. 4 and 7 and in Table 2. The values range from 16.4‰ to 25.2‰_{VSMOW} for $\delta^{18}\text{O}$ and from 1.0‰ to 3.1‰_{VDPB} for $\delta^{13}\text{C}$. All analyzed carbonate samples are depleted in heavy oxygen with respect to marine Cretaceous carbonate (Prokoph et al. 2008) (Fig. 7). This depletion is probably due to diagenesis and low-grade metamorphism. For most samples, we observe a systematic decrease of O isotope compositions toward the calc-mylonite (Fig. 7). According to data from the literature, $\delta^{18}\text{O}$ and $\delta^{13}\text{C}$ can, respectively, extend down to 13‰_{VSMOW} and −2‰_{VDPB} in PPV footwall rocks. The pattern of $\delta^{18}\text{O}$ depletion is the result of interaction within the fluid phase during the deformation (e.g., Burkhard et al. 1992; Rye and Bradbury 1988; Baumgartner and Rumble 1988). Sample PPV11–08, which shows a significant increase in ^{13}C , is characterized by a dark color (Fig. 2c) suggesting the presence of graphite and/or carbonaceous material (e.g., Van Der Pluijm 1991). However, isotopic effects of organic carbon on carbonate should be a lowering of $\delta^{13}\text{C}$ values, and this rules out this idea. Carbonaceous minerals are present, but rare in these rocks, and only a few detrital grains were observed using reflection optical microscopy. RSCM indicates peak temperatures ranging between 320 and 340 °C for an average of ten analyses in dolomitic limestone and calc-mylonite (Table 3).

Pelite hanging-wall characterization

The hanging-wall is mostly composed of Triassic pelite displaying a well-developed cleavage. A sharp color

Table 1 Dolomitic limestone and calc-mylonite mineralogical composition, in wt%, obtained with Rietveld refinement on XRD analyzes (Riet.) and with normative calculation on XRF analyzes (Norm.) (sample locations in Fig. 2)

Rocks	Samples	Method	D (m)	Calcite	Dolomite	Quartz	Σ	Rwp	GOF
Calc-mylonite	PPV11-08	Riet.	0.05	97.28 ± 1.8	2.43 ± 1.7	0.26 ± 0.6	100	15.45	5.09
	PPV11-07	Riet.	0.1	93.52 ± 1.7	6.36 ± 1.6	0.11 ± 0.5	100	14.46	4.79
		Norm.		91.9	5.6	0.3	97.8		
	PPV11-06	Riet.	0.3	97.27 ± 2.1	2.44 ± 2.0	0.28 ± 0.7	100	16.32	5.6
	PPV11-05	Riet.	0.4	86.19 ± 1.5	9.08 ± 1.5	4.73 ± 0.8	100	13.92	4.84
		Norm.		84.5	8	4.6	97.1		
Dol. limestone	PPV11-04	Riet.	2	85.29 ± 1.5	14.3 ± 1.4	0.41 ± 2.9	100	11.83	6.85
	PPV11-03	Riet.	5	24.9 ± 1.2	73.4 ± 1.3	1.7 ± 0.7	100	13.88	4.83
	PPV11-02	Riet.	10	95.93 ± 1.7	3.8 ± 1.7	0.27 ± 0.5	100	14.87	4.89
	PPV11-01	Riet.	15	90.06 ± 1.9	7.12 ± 1.7	2.82 ± 0.8	100	15.57	5.29
		Norm.		86.9	8.9	1.7	97.5		

D distance to thrust in meter, GOF goodness of fit in percent, Rwp weighted residual percent. Percentage approximations were obtained by the multiplication of the standard deviation given by the Topas software with the GOF, following the Taylor and Hinczak (2003) approach

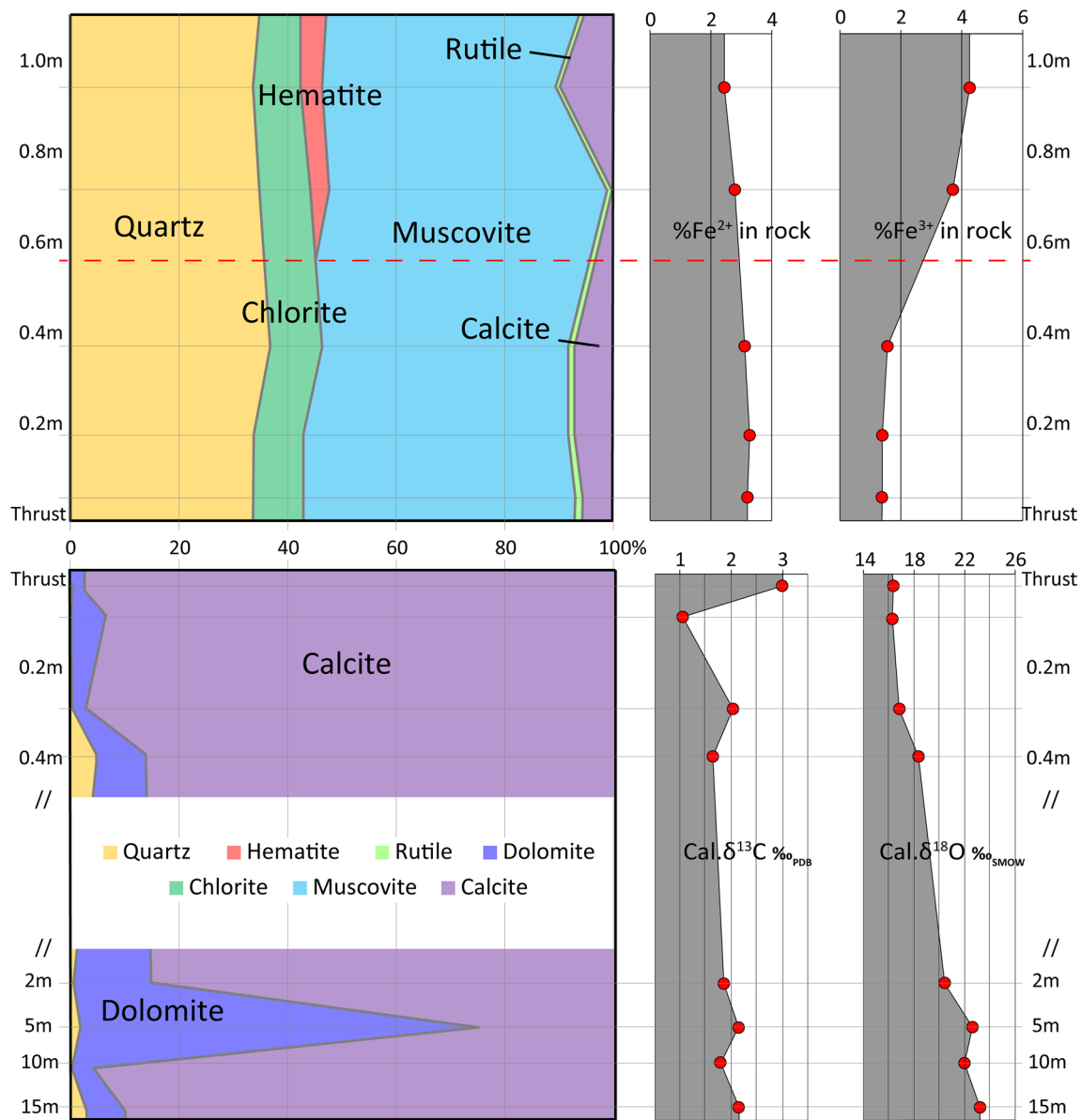


Fig. 4 Mineralogical composition of PPV thrust hanging-wall and footwall samples, from XRD Rietveld refinement and normative quantifications. Ferric and ferrous irons calculated from both XRF

(Appendix 2) and Mössbauer analyses (Table 5) are reported in the hanging-wall. Calcite $\delta^{13}\text{C}$ in ‰_{VPDB} and $\delta^{18}\text{O}$ in ‰_{VSMTOW} from isotopic analyses (Table 2) are reported in the footwall

change from red to green is observed ~1 m above the principal thrust, and 10–30 cm around the large faults (Fig. 2d). The transition between both colors is gradual but rapid, occurring over a few millimeters (Fig. 8a). As determined by SEM observations, Rietveld refinement and modal calculations, red pelite, and green pelite have similar mineralogical compositions with an average of 48 wt% of K-white mica, 34 wt% of quartz, 9 wt% of chlorite, 6 wt% of calcite (with one sample without calcite), 1 wt% of rutile, and few apatite crystals (Figs. 4, 8b, c; Table 4, Appendix 1). Quartz appears as more elongated crystals in the green pelite than in the red one, with long axis parallel

to cleavage. Hematite was only detected in the red pelite (4 wt%). Thus, the color change from red to green is attributed to hematite disappearance. This reflects a decrease in the iron content of the rock from 8% in the red pelite to 5% in the green pelite (XRF data in Appendix 2). Mössbauer spectroscopy shows that hematite, only composed of Fe^{3+} , incorporates 46–49% of the iron in the red pelite (Appendix 3). Furthermore, the red pelite appears as being more ferric (XFe^{3+} of 0.65 ± 0.05), while the green pelite is more ferrous (XFe^{3+} of 0.35 ± 0.05 , see Table 5). Fe^{2+} and Fe^{3+} percentages are calculated using both iron content (XRF analyses) and iron speciation (Mössbauer analyse).

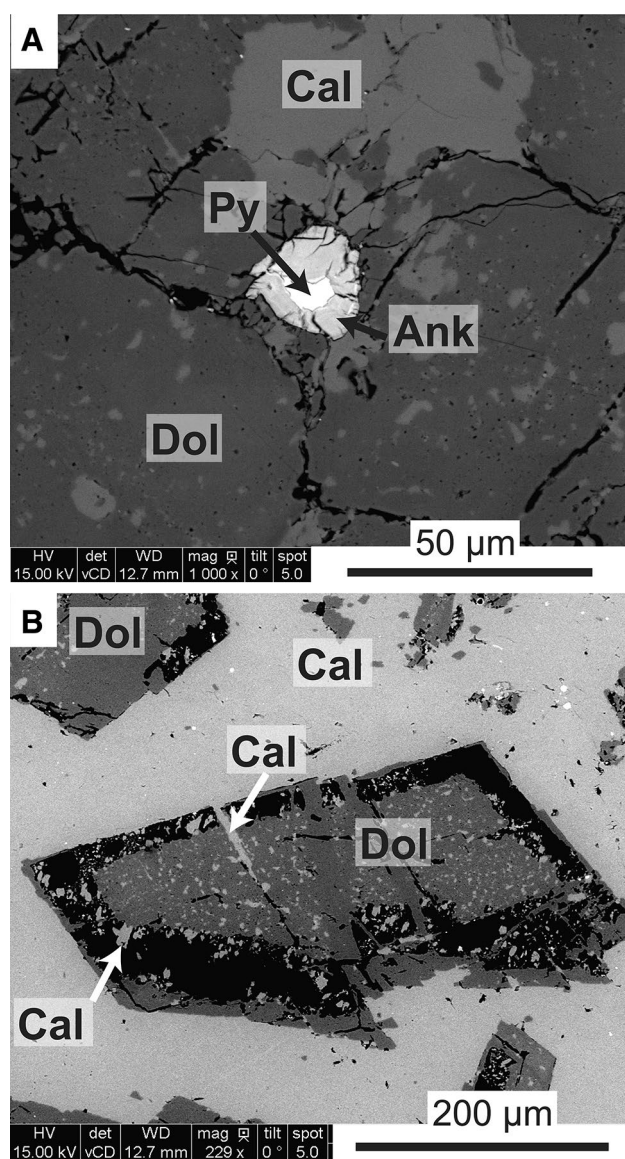


Fig. 5 Dolomitic limestone (PPV trust footwall; sample location in Fig. 2). **a** SEM images of pyrite crystal partly altered to ankerite (sample PPV11-01). **b** SEM images of dolomite crystal dissolution with calcite precipitation in cleavages and dissolution ghost (sample PPV11-02)

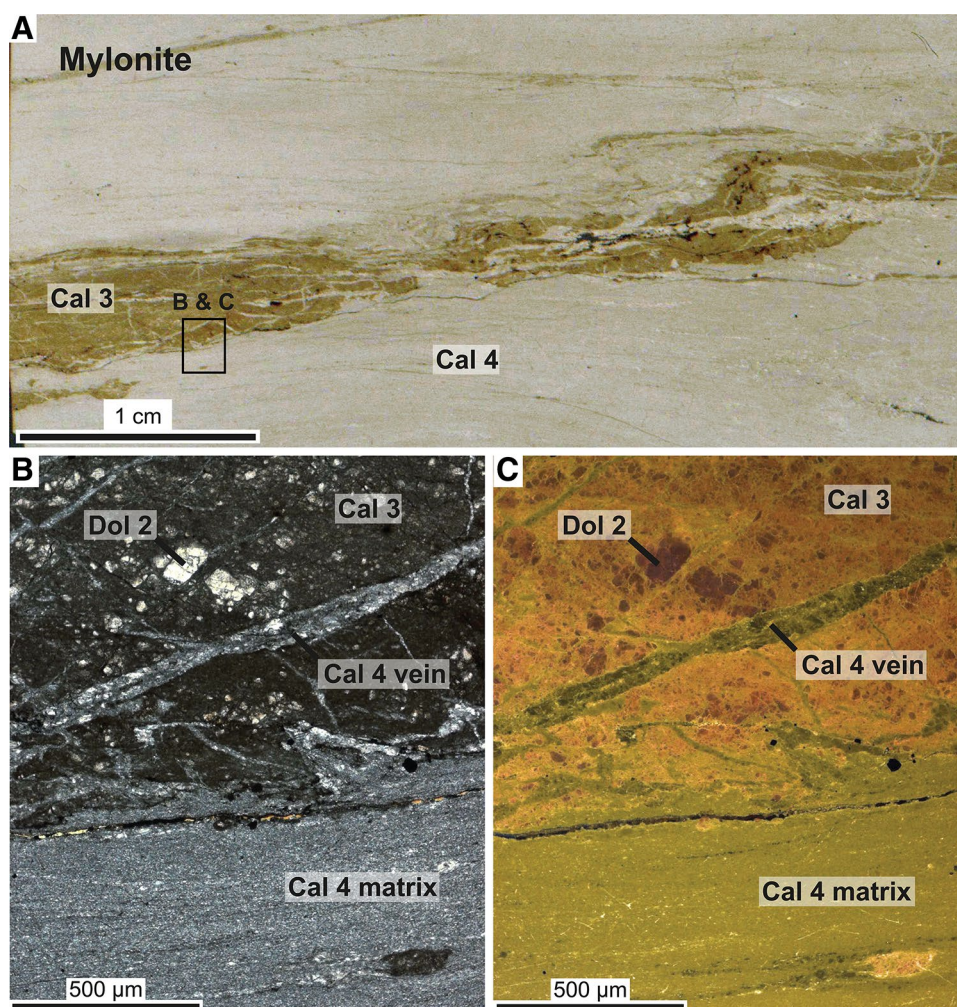
Fe^{2+} content in both the red and green pelites is close to 2.5 wt% (Fig. 4). However, Fe^{3+} decreases from 4 wt% in the red pelite to 1.5 wt% in the green one (Fig. 4).

Two types of white mica and two types of chlorite are recognized in both types of pelites. XFe^{3+} contents for phyllosilicates were estimated by subtracting the hematite iron content (Table 5). However, it was not possible to discriminate XFe^{3+} in mica and chlorite. Results appear similar for both the red and green pelites, with an average XFe^{3+} value equal to 0.34. However, XFe^{3+} for chlorite is not necessary the same as for muscovite (Bourdelle et al. 2013).

About 50 vol% of the rock matrix consists of small white mica grain aggregates with large deformed white mica flakes of few tens of micrometers underlying a well-defined cleavage (Grant 1989). Chemical compositions of the first type were plotted in an Al_2O_3 – K_2O –($\text{MgO} + \text{FeO}$) ternary diagram (Fig. 9a) and show a typical muscovite composition with a very small trend to more celadonite-rich mica. Muscovite data scarcity appears more important for the red pelite than for the green one; however, median structural formula used for mineralogical quantification (assuming $\text{XFe}^{3+} = 0.34$) is similar for both rocks, with $(\text{Si}_{3.16}\text{Al}_{0.83})(\text{Al}_{1.76}\text{Mg}_{0.12}\text{Fe}_{0.10}^{2+}\text{Fe}_{0.09}^{3+})\text{K}_{0.92}\text{Na}_{0.04}\text{O}_{10}(\text{OH})_2$ in red pelite and $(\text{Si}_{3.13}\text{Al}_{0.86})(\text{Al}_{1.75}\text{Mg}_{0.11}\text{Fe}_{0.15}^{2+}\text{Fe}_{0.13}^{3+})\text{K}_{0.92}\text{Na}_{0.03}\text{O}_{10}(\text{OH})_2$ in green pelite (Table 6; Electronic Supplementary Material 1). Large deformed chlorite-mica stacks occur equally in the red and green pelites. They may result from the biotite transformation as observed in redbeds from the Alps in low-grade metamorphism context (Tarantola et al. 2009). Chlorite grains in the matrix have probably a detrital origin, while chlorite filling shear veinlets or extension veinlets can be related to fault activity. Chlorite grain chemical compositions are plotted between clinocllore–daphnite, sudoite, and amesite components in an FeMg – Si – Al ternary diagram (Fig. 9b). Structural formulas were calculated using XFe^{3+} predicted by the Vidal et al. (2005) model. As for white mica, chlorite data scarcity appears more important for the red pelite, and median structural formulas are similar for both rocks, with $(\text{Si}_{2.72}\text{Al}_{1.28})[\text{Al}_{1.53}\text{Mg}_{2.09}\text{Fe}_{1.78}^{2+}\text{Fe}_{0.40}^{3+}]\text{O}_{10}(\text{OH})_8$ in the red pelite and $(\text{Si}_{2.74}\text{Al}_{1.26})[\text{Al}_{1.51}\text{Mg}_{2.23}\text{Fe}_{1.63}^{2+}\text{Fe}_{0.50}^{3+}]\text{O}_{10}(\text{OH})_8$ in the green pelite (Table 6; Electronic Supplementary Material 2). Chlorite thermometry yields to formation temperatures between 230 ± 50 and 315 ± 50 °C with a median value of 270 ± 50 °C (Table 6). Despite minor variations, no significant difference is observed between chlorite temperatures of the red and green pelites.

The $\delta^{18}\text{O}$ values of quartz and $\delta^{18}\text{O}$ and δH values of chlorite from two veins from the hanging-wall are given in Table 7. The two veins give similar $\delta^{18}\text{O}$ values of 11.3 and 11.4‰ $_{\text{VSMOW}}$ for quartz and of 18.2 and 17.8‰ $_{\text{VSMOW}}$ for chlorite. For δH , chlorite from both analyzed veins gives similar values of -60 and -61 ‰ $_{\text{VSMOW}}$ (Table 7). The similarity in $\delta^{18}\text{O}$ and δH compositions of chlorite and quartz in the two veins suggests that the isotopic compositions are homogeneous in veins at the outcrop scale. Therefore, veins might have been in isotopic equilibrium with the mineralizing fluid, and the isotopic values can be used to calculate the temperature of vein formation as well as the isotopic composition of the fluid. Oxygen isotope thermometry was applied to the quartz–chlorite mineral pairs (Lacroix and Vennemann 2015), giving formation temperatures of quartz–chlorite veins of 305 and 343 °C (Table 7). While a statistical treatment to evaluate an absolute uncertainty on

Fig. 6 Calc-mylonite petrography (PPV thrust footwall PPV11-07; sample location in Fig. 2). Optical (a) and cathodo-luminescence (b) microscope images of calc-mylonite showing two calcite generations (Cal3 and Cal4) and dolomite (Dol2) crystal remains



the temperature is not considered in Lacroix and Vennemann (2015), the value of uncertainty is not expected to exceed ± 50 °C.

Discussion

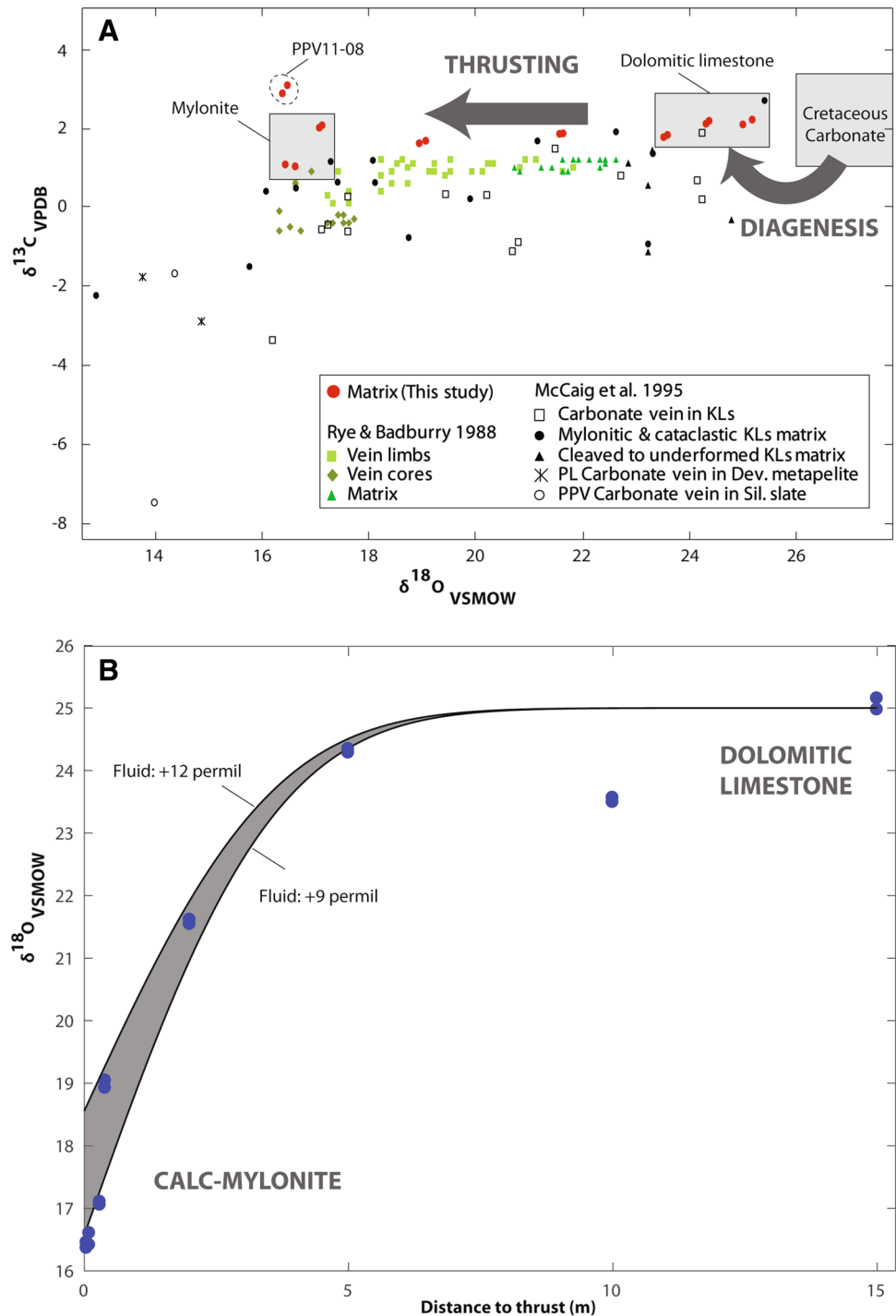
Water–rock interactions and deformation in the dolomitic limestone footwall

The dolomitic limestone located below the PPV thrust experienced two stages of mylonitization produced by the successive activities of the Gavarnie and PPV thrusts (Grant 1990; Banks et al. 1991). The calc-mylonite foliation affects carbonates in the footwall damage zone up to 1–2 m below the thrust contact. It can be related to both mechanical grain size reduction process and interaction with fluids (Fig. 4). Indeed, several calcite and dolomite generations are recognized by CL microscopy. Cal1 has probably a sedimentary origin. Cal2 is associated with Dol1; it was probably formed by the diagenetic recrystallization of Cal1

or by crystallization from diagenetic fluid flow. Cal3 may be diagenetic (cogenetic with Cal2 and Dol1) or more probably linked to diffusion/recrystallization processes affecting Cal1 during PPV thrusting. Dolomite dissolution observed by SEM (Fig. 5b) suggests that dolomite was not stable during the late burial diagenesis and/or thrusting. Cal4 veins are post-Cal3 and may be related to the last PPV thrusting episode (Fig. 6b, c). However, attributing carbonate generations to structural events is not straightforward, because the Gavarnie–PPV thrust activity shows several stages formed under the same stress field and likely corresponding to a continuous deformation.

McCaig et al. (1995) investigated the Sr fractionation along PPV and other sections of the Gavarnie-thrust-related faults. They suggest that the PPV calc-mylonite has a higher permeability than the dolomitic limestone protolith, enabling to channelize syntectonic fluid flow along the core zone with limited interaction exchange with the footwall. Carbonate mylonitization is a common process when temperature reaches 200–400 °C, resulting from plastic deformation mechanism (mainly calcite

Fig. 7 **a** Isotopic compositions of PPV footwall bulk rock calcites in red (sample location in Fig. 2) and of carbonaceous samples from Rye and Bradbury (1988) in green and McCaig et al. (1995) in black. $\delta^{18}\text{O}$ in ‰ VSMOW , $\delta^{13}\text{C}$ in ‰ VPDB . Marine Cretaceous carbonates area from Prokoph et al. (2008). Schematic isotopic exchange pathways for calcite, from an initial marine rock undergoing diagenesis and then buffered with a fluid flow. **b** Non-linear trend in $\delta^{18}\text{O}$ values along the profile from carbonates footwall suggesting the presence of an alteration isotope front during the PPV fault activity. To predict the different parameters controlling the dispersive diffusive front and the time-integrated fluid flux, a similar procedure as proposed by Badertscher et al. (2002) with Eq. (1) was applied. The parameters ν and ω are obtained from fitting Eq. (1) to measured data within the footwall, using fluid composition of 9 (McCaig et al. 1995)–11‰ (our data)



twinning) (Burkhard 1990; Bestmann et al. 2000; Ferrill et al. 2004; Schenk et al. 2005; Molli et al. 2011) and dynamic recrystallization with grain size reduction (e.g., Knipe 1989; Busch and van der Pluijm 1995; Bresser et al. 2001; Ferrill et al. 2004; Ebert et al. 2007; Molli et al. 2011). The mylonitization context in the PPV thrust (i.e., rock type and metamorphic conditions) is very similar to that of the Gavarnie thrust (Knipe and McCaig 1994), the

Morcle nappe (e.g., Kirschner et al. 1995; Herwegh et al. 2008) or the Glarus thrust in the Swiss Alps (e.g., Pfiffner 1982, 1985; Burkhard et al. 1992). Ebert et al. (2007) described calcite grain size reduction and twin density increase in the Glarus mylonites under temperatures of about 300 °C. Such textures suggest that carbonates were deformed plastically by fluid-assisted dislocation creep and dynamic recrystallization. Similar observations are

Table 2 Dolomitic limestone and calc-mylonite carbon and oxygen isotope data (sample location in Fig. 2)

Rock	Samples	D (m)	Calcite	
			$\delta^{13}\text{C}$ ‰ _{VPDB}	$\delta^{18}\text{O}$ ‰ _{VSMOW}
Dolomitic limestone	PPV11_01A	15	2.09	24.97
	PPV11_01B	15	2.21	25.15
	PPV11_02A	10	1.77	23.49
	PPV11_02B	10	1.82	23.56
	PPV11_03A	5	2.18	24.34
	PPV11_03B	5	2.10	24.28
	PPV11_04A	2	1.86	21.61
Calc-mylonite	PPV11_04B	2	1.85	21.54
	PPV11_05A	0.4	1.67	19.04
	PPV11_05B	0.4	1.61	18.92
	PPV11_06A	0.3	2.00	17.05
	PPV11_06B	0.3	2.06	17.10
	PPV11_07A	0.1	1.03	16.60
	PPV11_07B	0.1	1.08	16.41
	PPV11_08A	0.05	3.08	16.45
	PPV11_08B	0.05	2.87	16.36

Standard deviation of results is less than 0.1‰. D: distance to thrust in meters

Table 3 Raman spectroscopy of carbonaceous material (sample location in Fig. 2)

Rock	Samples	RA1	SD	Num- ber of spectra	T (°C)
		parameter Mean			
Dol. Limest.	PPV11-01	0.6500	0.0079	10	338 (10)
Calc-mylonite	PPV11-08	0.6379	0.0041	10	322 (6)

RA1 parameter in Lahfid et al. (2010); SD: RA1 standard deviation

made in the PPV mylonites (Fig. 6), suggesting that similar deformation mechanisms played a key role.

The isotopic compositions of metamorphic rocks are controlled by numerous factors including: the protolith composition, the effects of devolatilisation reactions (controlled by *P* and *T*), fluid sources and fluid/rock ratios, and the temperature and kinetics of exchange (Ferry and Dipple 1991). The oxygen isotope composition of carbonate depends on the $\delta^{18}\text{O}$ signature of the fluid, the precipitation temperature, and the oxygen fractionation between the fluid and the calcite (O'Neil et al. 1969; Friedman and O'Neil 1977). In the PPV thrust fault zone, dolomitic limestone samples have calcite $\delta^{18}\text{O}$ values ranging from 23.5 to 25.2‰_{VSMOW} and $\delta^{13}\text{C}$ of 2.0‰_{VPDB} (Figs. 4, 7; Table 2). These values are slightly lower than those of unaltered Cretaceous marine sediments, whose typical $\delta^{18}\text{O}$ value is higher than 26‰_{VSMOW} (Veizer et al. 1999; Prokoph et al. 2008). Such depletion can be interpreted as the re-equilibration of the sediment during the burial diagenesis prior to calc-mylonite

formation. Cretaceous diagenetic marine carbonates from the Cinca Valley near Bielsa (Rye and Bradbury 1988) or the Plan de Larri and PPV (McCaig et al. 1995) have similar $\delta^{18}\text{O}$ values.

Calc-mylonite samples display lower $\delta^{18}\text{O}$ values ranging between 16.4 and 17.1‰_{VSMOW} and $\delta^{13}\text{C}$ values ranging from 1.0 to 3.1‰_{VPDB} (Figs. 4, 7; Table 2). Using published data, $\delta^{18}\text{O}$ and $\delta^{13}\text{C}$ of this rock can reach 13‰_{VSMOW} and −3‰_{VPDB}, respectively (Fig. 7; Rye and Bradbury 1988; McCaig et al. 1995). It is unlikely that decarbonation processes generated the observed $\delta^{18}\text{O}$ depletion close to the thrust, because it would imply a temperature higher than 550 °C. The carbonate breakdown $\text{CaCO}_3 \rightarrow \text{CO}_2 + \text{CaO}$ associated with CO_2 devolatilization occurs at this temperature (e.g., Baumgartner and Valley 2001). CO_2 devolatilization would have a dramatic effect on the O- and C-isotope composition of residual carbonate. However, in this study, we clearly establish that the temperature of calc-mylonite formation occurred at ~320 °C. The observed trend is probably caused by fluid–rock interactions related to the PPV thrust activity (see below). All $\delta^{13}\text{C}$ values are in the typical range of unaltered marine limestone (Hudson 1977; Nelson and Smith 1996; Veizer et al. 1999), except for the PPV11–08 sample, which has a $\delta^{13}\text{C}$ value of 3‰_{VPDB}. ^{13}C -enrichment is observed for sample PPV11–08. This sample is darker color that could be related to the presence of graphite. The large positive shift in ^{13}C values could be explained either by (1) the contribution of C-rich metamorphic fluid coming from deeper conditions or (2) local change in sedimentary environment during the deposition of carbonate. However, the lack of CO_2 -rich inclusions (Banks et al. 1991; Grant et al. 1990) does not suggest the presence of CO_2 -rich fluids during deformation. Therefore, we assume this ^{13}C value as a local heterogeneity within the Cretaceous limestones which are also sometimes rich in pyrite (Banks et al. 1991).

Oxygen- and carbon-isotope compositions decrease toward the calc-mylonite and the thrust fault surface, where calcite recrystallization took place. Similar trends were observed in other shear zones or mylonites worldwide (e.g., in the Glarus thrust; Abart et al. 2002), and are attributed to a partial or total re-equilibration of calcite with an external fluid during calc-mylonite formation (e.g., Burkhard et al. 1992; Baumgartner and Valley 2001). The lower $\delta^{18}\text{O}$ composition within the calc-mylonite layer is generally assumed to be in isotopic equilibrium with the fluid that flowed through the porous media. Therefore, its $\delta^{18}\text{O}$ composition can be approximated using the inferred temperature of calc-mylonite formation and the calcite–water oxygen isotope fractionation factor of O'Neil et al. (1969) refined by Zheng (1999). Among other fractionation factors (see Beaudoin and Therrien 1999 for a review), the Matsuhisa et al. (1979) and Cole and Ripley (1998) calibrations were applied to chlorite

Fig. 8 Pelite (PPV thrust hanging-wall; sample location in Fig. 2). **a** Scanned thin section of PPV12-02A sample showing contact between red and green foliated pelites matrix and veins of oxidized calcite + chlorite. **b** SEM image of red pelite PPV12-06B showing presence of hematite. **c** SEM image of green pelite PPV12-05 showing presence of chlorite veinlets but without hematite. Key: *Ap* apatite, *Chl* chlorite, *Hem* hematite, *Ms* muscovite, *Qz* quartz, *Rt* Rutile

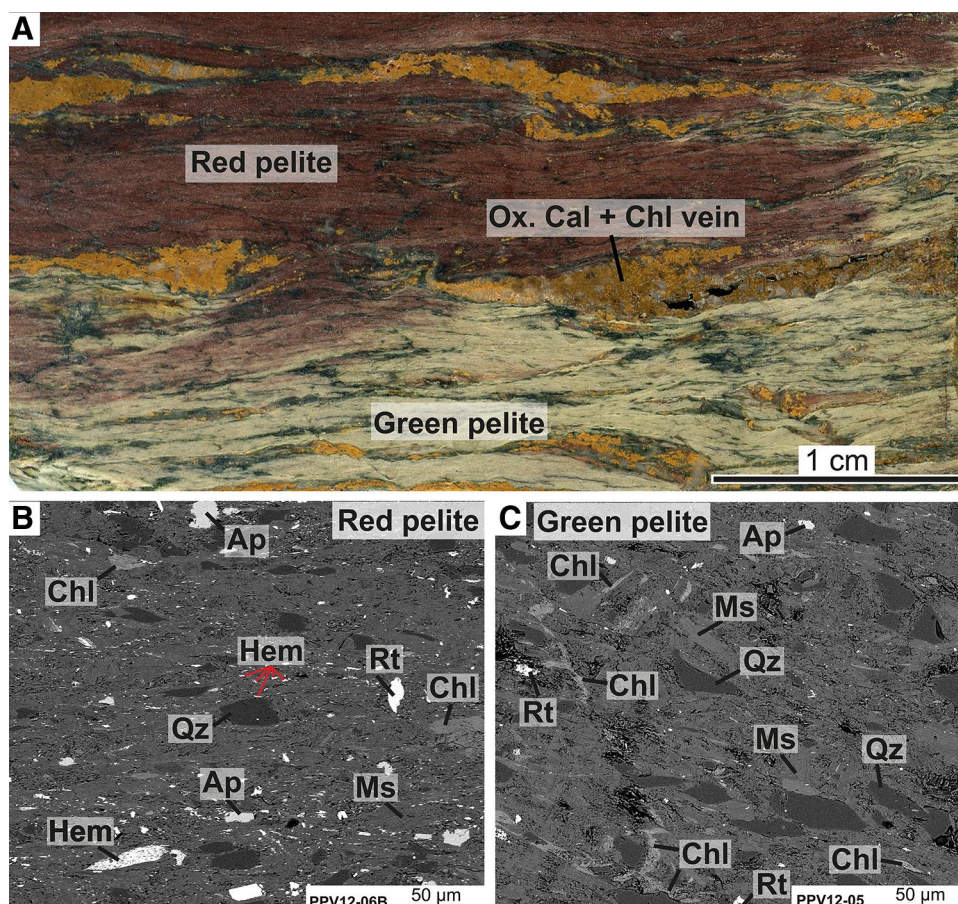


Table 4 Green and red pelites mineralogical composition, in wt%, obtained by Rietveld refinement on XRD analyzes (Riet.) and by normative calculation on XRF analyzes (Norm.) (sample locations in Fig. 2)

Rocks	Samples	D (m)	Method	Apatite	Calcite	Chlorite	Hematite	Muscovite	Quartz	Rutile	Σ	Rwp	GOF
Red pelite	PPV12-07	1.2	Riet.		5.2 ± 0.9	7.4 ± 2.2	4.7 ± 0.6	46.8 ± 2	35.3 ± 1.5	0.7 ± 0.5	100	7	3.6
			Norm.	0.44	3.54	8.73	4.38	49.19	31.65	0.73	98.7		
	PPV12-06	0.9	Riet.		9.7 ± 2.5	9 ± 1.9	3.7 ± 0.5	43 ± 2.1	33.9 ± 0.2	0.8 ± 0.4	100	6.7	3.6
			Norm.	0.44	1.74	10.10	3.93	48.11	33.18	0.76	98.3		
	PPV12-01	0.7	Riet.		0 ± 0	9.4 ± 2.3	3.5 ± 0.6	51.2 ± 2	35 ± 1.5	1 ± 0.6	100	7.3	3.7
			Norm.	0.45	0.78	9.80	3.63	51.99	31.37	0.83	98.9		
Green pelite	PPV12-03	0.5	Riet.		7.2 ± 0.9	9.7 ± 2	0 ± 0	45.2 ± 2	37 ± 1.5	1 ± 0.5	100	8.1	3.9
			Norm.	0.4	6.7	11.8	0.7	45.7	33.1	0.6	99.0		
	PPV12-04	0.3	Riet.		6.9 ± 0.9	9.2 ± 2.2	0 ± 0	48.5 ± 2.1	34.3 ± 1.5	1.1 ± 0.6	100	8.2	4
			Norm.	0.4	6.1	12.6	0.8	46.6	32.7	0.6	99.9		
	PPV12-05	0.1	Riet.		5.5 ± 1	9.1 ± 2.5	0 ± 0	50.2 ± 2.2	34 ± 1.7	1.1 ± 0.6	100	8.6	4.2
			Norm.	0.5	4.2	12.2	0.8	51.1	30.9	0.7	100.3		

D: distance to thrust. GOF: goodness of fit in percent. Rwp: weighted residual percent. Percentage approximations were obtained by the multiplication of the standard deviation given by the Topas software with the GOF, following the Taylor and Hinczak (2003) approach

and quartz couples from hanging-wall veins. These veins and calc-mylonite are assumed to be contemporary with thrusting (Trincal et al. 2015). As demonstrated in previous section, the new oxygen isotope values obtained on chlorite,

quartz, and calcite from hanging-wall veins and temperatures are in agreement with the flow of a fluid with $\delta^{18}\text{O}$ of $\sim 11\text{‰}$ VSMOW (Table 7). Such an O composition is generally associated with metamorphic water or with heated formation

Table 5 Mössbauer hyperfine parameters with *CS* isomer shift, *QS* quadrupole splitting, *H* hyperfine field, and *RA* relative abundance

Samples		CS (mm/s)	QS (mm/s)	H (kOe)	RA (%)	
PPV12-06	Fe ²⁺	1.11	2.9		9	Phyllosilicates
Red pelite	Fe ³⁺	0.36	0.46		12	(XFe ³⁺ = 0.37)
(XFe ³⁺ = 0.68)	Fe ²⁺	0.99	2.11		7	
	Fe ²⁺	1.08	2.58		16	
	Fe ³⁺	0.44	1.01		7	
		0.37	−0.107	512	49	Hematite
PPV12-01	Fe ²⁺	1.11	2.64		38	Phyllosilicates
Red pelite	Fe ³⁺	0.27	0.64		11	(XFe ³⁺ = 0.30)
(XFe ³⁺ = 0.62)	Fe ³⁺	0.57	0.81		5	
		0.39	−0.105	515	46	Hematite
PPV12-03	Fe ²⁺	1.11	2.64		55	Phyllosilicates
Green pelite	Fe ³⁺	0.31	0.64		31	(XFe ³⁺ = 0.38)
(XFe ³⁺ = 0.38)	Fe ³⁺	0.51	1.4		7	
	Fe ²⁺	1.15	2.13		7	
PPV12-04	Fe ²⁺	1.08	2.62		62	Phyllosilicates
Green pelite	Fe ³⁺	0.31	0.58		27	(XFe ³⁺ = 0.34)
(XFe ³⁺ = 0.34)	Fe ³⁺	0.42	1.13		7	
	Fe ²⁺	1.11	1.81		4	
PPV12-05	Fe ²⁺	1.07	2.64		58	Phyllosilicates
Green pelite	Fe ³⁺	0.34	0.59		30	(XFe ³⁺ = 0.35)
(XFe ³⁺ = 0.35)	Fe ³⁺	0.5	1.25		5	
	Fe ²⁺	0.97	1.9		7	

XFe³⁺ = Fe³⁺/(Fe²⁺+Fe³⁺) calculated in the rock samples and in phyllosilicates only (removing hematite Fe³⁺ content to the total rock) (sample location in Fig. 2)

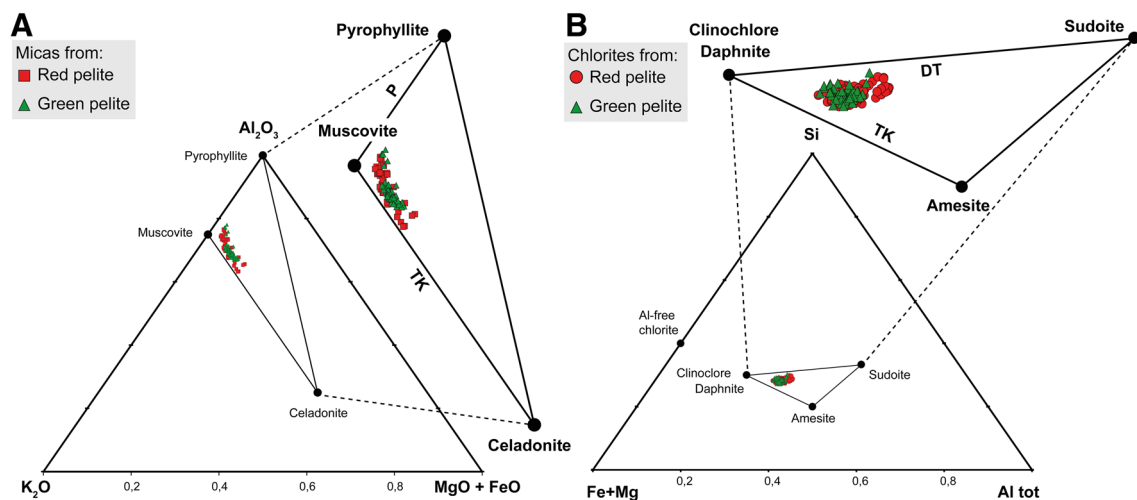


Fig. 9 Chemical composition of phyllosilicates from the Triassic pelites of the PPV thrust hanging-wall (sample location in Fig. 2). **a** Al_2O_3 – K_2O – $\text{MgO}+\text{FeO}$ ternary plot of matrix micas with muscovite ($\text{Si}_3\text{Al}_3\text{K}(\text{OH})_2$); celadonite ($\text{Si}_4\text{Al}(\text{Mg},\text{Fe})\text{K}(\text{OH})_2$); pyrophyllite ($\text{Si}_4\text{Al}_2\text{O}_{10}(\text{OH})_2$); *TK* Tschermak substitution, *P* pyrophyllitic

substitution. **b** FeMg – Si – Al ternary plot of chlorites from matrix with amesite ($(\text{Si}_2\text{Al}_2)[\text{Al}_2(\text{Fe},\text{Mg})_4]\text{O}_{10}(\text{OH})_8$); clinochlore ($(\text{Si}_3\text{Al})[\text{AlMg}_5]\text{O}_{10}(\text{OH})_8$); daphnite ($(\text{Si}_3\text{Al})[\text{AlFe}_5]\text{O}_{10}(\text{OH})_8$); sudoite ($(\text{Si}_3\text{Al})[\text{Al}_3\text{Fe}_3]\text{O}_{10}(\text{OH})_8$); *DT* di-trioctahedral substitution

water (Longstaffe 1987); it clearly excludes the presence of meteoric fluids, which have negative $\delta^{18}\text{O}$ values (Savin and Lee 1988; Sharp 2009). However, the work of McCaig et al.

(1995) based on Sr isotope composition of the same calc-mylonite section studied here suggests the Triassic rocks as source. According to Nesbitt and Muehlenbachs (1995),

Table 6 Mica and chlorite median structural formulas from red and green pelite matrix samples obtained by microprobe analyses (Appendices 4, 5). *n*: number of analyses, SD: standard deviation.

$X_{Mg} = Mg/(Fe + Mg)$. Chlorite T and XFe^{3+} data were estimated by the Vidal et al. (2005, 2006) method. Mica XFe^{3+} data were obtained by phyllosilicate Mössbauer analyses

Wt%	Red pelite muscovites		Green pelite muscovites		Red pelite chlorites		Green pelite chlorites	
	(<i>n</i> = 59)	SD	(<i>n</i> = 67)	SD	(<i>n</i> = 113)	SD	(<i>n</i> = 63)	SD
SiO ₂	47.47	1.19	47.10	0.82	26.49	0.81	26.72	0.68
TiO ₂	0.28	0.17	0.34	0.43	0.04	0.04	0.03	0.18
Al ₂ O ₃	33.13	2.05	33.00	1.46	23.14	0.75	22.91	0.62
FeO	1.80	1.08	2.62	0.74	24.43	1.88	23.01	1.44
MnO	0.00	0.01	0.00	0.31	0.05	0.08	0.04	0.01
MgO	1.26	0.70	1.15	0.27	13.51	1.51	14.59	1.04
CaO	0.01	0.02	0.04	0.03	0.04	0.03	0.06	0.04
Na ₂ O	0.29	0.25	0.21	0.35	0.01	0.02	0.00	0.01
K ₂ O	10.85	0.37	10.85	0.50	0.07	0.19	0.03	0.12
Cr ₂ O ₃	0.01	0.02	0.02	0.02				
Total	95.78	0.70	95.70	16.75	88.04	1.09	87.66	0.93
11 oxygens					14 oxygens			
Si	3.16	0.08	3.13	0.05	2.72	0.03	2.74	0.03
Al	2.62	0.15	2.60	0.10	2.81	0.07	2.78	0.08
Al ^{IV}	0.83	0.08	0.86	0.05	1.28	0.03	1.26	0.03
Al ^{VI}	1.76	0.08	1.75	0.06	1.53	0.07	1.51	0.06
Mg	0.12	0.07	0.11	0.03	2.09	0.22	2.23	0.15
Fe ²⁺	0.10	0.06	0.15	0.04	1.78	0.29	1.63	0.28
Fe ³⁺	0.09	0.05	0.13	0.04	0.40	0.19	0.50	0.21
K	0.92	0.04	0.92	0.05				
Na	0.04	0.03	0.03	0.04				
X_{Mg}	0.55		0.44		0.54		0.58	
T °C					277	38	265	36
XFe^{3+}	0.34		0.34		14	7.7	18	9.2

Table 7 Isotopic analyses from PPV samples (sample locations in Fig. 2)

Sample	Mineral	$\delta^{18}O_{\text{mineral}}$	$\delta^{18}O_{\text{water}}$	$\Delta^{18}O_{\text{qtz-chl}}$	<i>T</i> (°C)	$\delta H_{\text{mineral}}$	δH_{water}
PPV11-XX	Quartz	18.21 ± 0.14	12.0 ^a	6.93	305 ^e		
	Chlorite	11.28 ± 0.16	11.4 ^b			−60.2	−32.2 ^c
PPV11-26	Quartz	17.82	11.6 ^a	6.43	343 ^e		
	Chlorite	11.39	11.5 ^b			−61	−33.0 ^c
PPV11-08	Calcite	16.45	11.2 ^d				

$\delta^{18}O$ in ‰_{VSMOW}, $\delta^{13}C$ in ‰_{V-PDB} and δH in ‰_{VSMOW}. Quartz (qtz) and chlorite (chl) from hanging-wall veins. Calcite (cc) from footwall calc-mylonite. Fluid properties calculated from ^a Matsuhisa et al. (1979); ^b Cole and Ripley (1998); ^c Graham et al. (1987); ^d Zheng (1999); ^e Lacroix and Vennemann (2015) calibrations

carbon or oxygen isotopic data do not permit to distinguish a metamorphic fluid in equilibrium with distant basement from a sedimentary formation fluid equilibrated at metamorphic conditions. To address this question, the δH composition of the fluid was calculated from the chlorite and quartz δH using the calibration of Graham et al. (1987). A negative value about −32‰ was found (Table 7), suggesting a water

in equilibrium with deeper basement rocks under greenschist facies metamorphic conditions, in agreement with the paleo-hydrological model proposed by Lacroix et al. (2014) for the south-Pyrenean thrust system, note that these authors used the term of metamorphic fluid but not in the sense of a dehydration water.

The non-linear trend in $\delta^{18}\text{O}$ values along the profile from carbonates footwall toward the calc-mylonite suggests the presence of an alteration front during the PPV fault activity (Fig. 7b) (Bickle and McKenzie 1987; McCaig et al. 1995; Badertscher et al. 2002; Baumgartner and Valley 2001). Based on Sr isotope, McCaig et al. (1995) investigated the isotopic exchange, parallel to the thrust along calc-mylonite through advective and diffusive fluid-flow models. In this section, we address its lateral effect, i.e., isotopic exchange perpendicular to fault zone. The theory predicts that coupled advective and diffusive transport result in the migration of an isotopic front within porous media (here Cretaceous carbonate). However, the dispersion processes could be influenced by the tortuosity of the porous media. To predict the different parameters controlling the dispersive diffusive front and the time-integrated fluid flux, we applied a similar procedure as proposed by Badertscher et al. (2002) with Eq. (1):

$$R(x, t) = R_f - (R_f - R_i) \times \operatorname{erfc} \frac{x + \omega}{2\sqrt{v}} \quad (1)$$

where R is the O isotope composition of the rock at x meters from the contact and at time t (in second), and R_f and R_i are the isotope O composition of the rock and fluid, respectively. v ($v = D^*t$) corresponds to the length of dispersion/diffusion, where D is the effective diffusion/dispersion coefficient and t is the time in second. The parameter ω ($\omega = v^*t$) represents the advective displacement of the front compared to its initial position, where v is the mean particle velocity within porous media. The parameters v and ω are obtained from fitting Eq. (1) to our measured data within the footwall (Fig. 7b). The best-fit curve is obtained for v and ω values of 4 and 0.3 m, respectively. The obtained ω value allows to calculate the Time-Integrated Fluid Flux (TIFF) from the calc-mylonite to the footwall using Eq. (2):

$$\text{TIFF} = \omega \times K_d \quad (2)$$

where K_d is the solid/fluid partition coefficient of oxygen. Considering K_d of 1.85 as calculated by McCaig et al. (1995) and our estimated ω of 0.3, the TIFF is $0.54 \text{ m}^3/\text{m}^2$. Such a fluid flux is several magnitude orders slower than $\sim 1670 \text{ m}^3/\text{m}^2$, the flux thrust parallel to the calc-mylonite along the Gavarnie thrust fault estimated using Sr (McCaig et al. 1995). A similar difference in fluid flow parallel and perpendicular to mylonites was documented in the case of the Glarus thrust (Badertscher et al. 2002).

Dispersivities/diffusivities are generally strongly influenced by effective dispersion/diffusion coefficient of a species in the pore fluid medium. The general diffusivity of a specie is given by Eq. (3):

$$D = \tau \times \phi \times D_0 \quad (3)$$

where τ is the tortuosity and ϕ porosity. Porosity does not significantly changes over the calc-mylonite. However,

tortuosity is strongly influenced by strain (Zhang and Cox 2000; Kim and Inoue 2003). In the case of PPV mylonite, strain is marked by the formation of an anisotropic fabric (e.g., foliation, pressure solution, and fish clast) which tends to be parallel to the fault zone with increasing stress. The presence of tectonic fabrics could create sufficient anisotropy tortuosity (with important tortuosity oblique to the thrust and low tortuosity parallel to the thrust) (Kim and Inoue, 2003) to generate the TIFF difference between parallel and oblique to the thrust.

Fluid–rock interaction and deformation in the Triassic redbeds

Hematite represents about 50 wt% of the total iron from the PPV thrust footwall red pelite, the remaining iron being distributed in chlorite ($\sim 35\%$) and muscovite ($\sim 15\%$, see Table 5). The greenish pelite interval, up to 1 m thick, displays the same mineralogical composition than the reddish one, except for hematite that is totally absent (Table 4). Phyllosilicates have not been affected during thrusting, but the iron oxidation state discrimination between both mica and chlorite could not be ascertained by Mössbauer spectroscopy. Hematite disappearance suggests a dissolution reaction driven by fluid flow infiltrating the pelite perpendicularly to the thrust and to the secondary faults (e.g., Wigley et al. 2013; Abd Elmola et al. 2017). The hematite dissolution to form the reduced green pelites implies a decrease in the total amount of FeO from 8 to 5% (Appendix 2) and a major change in the redox conditions (McCaig et al. 1995). This dissolution of hematite and the smooth color transition between the red and green pelites suggest an active reaction front that would have been controlled by advective fluid flow penetrating around the main thrust and the secondary faults, probably following the cleavage surfaces. A similar model was described in the Entrada Sandstone (US), where hematite dissolution was explained by interaction with a reducing brine (Wigley et al. 2012, 2013). In the context of the PPV thrust, the circulating fluid was probably reduced by interaction with Devonian basement rock or with Silurian graphitic slates (McCaig et al. 2000c).

Quartz–chlorite faults and veins (Fn3 and V5 in Grant 1992) associated with the PPV thrust reactivation by spreading/gliding (i.e., corresponding to the latest stage of emplacement) are contemporaneous to pelite discoloration. These low-angle (synthetic) R-shear normal faults are associated with the development of planar and sigmoidal, south dipping quartz–chlorite–calcite extension veins and gashes. These veins formed as geodic cavities filled by euhedral quartz grains. Microthermometry of fluid inclusions performed by crush leach method on these quartz veins reveals temperatures of 250–300 °C (Grant et al. 1990; Banks et al. 1991; McCaig et al. 2000b). These data are consistent with

the temperature of 320 ± 30 °C determined for the same quartz–chlorite veins, using oxygen isotope fractionation between quartz and chlorite (Lacroix and Vennemann, 2015). These results are also consistent with chlorite thermometry and temperatures inferred by RSCM technique performed in this study. Furthermore, oscillatory zoning pattern chlorites identified in shear veins associated with Fn3 faults (Grant 1989) attest temperature variations from 310 ± 50 to 400 ± 50 °C. These variations are associated with seismic-valve behavior of the thrust during crystallization (Trincal et al. 2015). According to these independent approaches, the temperature of the mineralizing fluid can be estimated to 320 °C.

Redox conditions of the fluid are likely to be a critical parameter for hematite stability in host rock. They were tested with PHREEQC 2.15 program simulations (Parkhurst 1995; Parkhurst and Appelo 1999). Starting with the composition of rain water (representing the water at the time of the pelite sedimentation) (data from Appelo and Postma 2004), a pore-water composition in equilibrium at 300 °C with the red pelite mineralogy (Table 4) was calculated. A temperature of 300 °C was chosen instead of 320 °C, because PHREEQC thermodynamic database is more accurate for 300 °C. Then, several redox conditions were used to simulate the chemical reactions occurring between the interstitial fluid and the red pelite minerals. The probability for iron oxides/hydroxides, carbonate and sulfur, as well phyllosilicates to precipitate was calculated. According to the simulation

(Fig. 10, Appendix 4), the fluid allows hematite precipitation in oxidizing condition ($p_e \geq 5$) and its dissolution in more reducing conditions ($p_e \leq 4.9$). p_e is a redox expression that may be converted in Eh via a temperature-dependent Nernst relationship. Magnetite is the iron-rich mineral predicted in intermediate reducing conditions ($4.9 \geq p_e \geq -5.8$). In highly reducing conditions, magnetite is progressively replaced by chlorite. According to numerical modeling performed in this study, the presence of newly formed iron-rich chlorite in pelite veins instead of magnetite indicates very anoxic fluid-flow conditions ($p_e < -5.9$). A fluid can become more reducing crossing-layer rich in organic matter, such as the Silurian phyllites exposed in the Gavarnie thrust hanging-wall, a few tens of meters from the studied PPV outcrop. However, the PPV thrust does not intersect these rocks. This may involve a branching between both the Gavarnie thrust and the PPV thrust (Fig. 1c). Furthermore, during the Gavarnie thrust formation, the Silurian would have been in contact with Cretaceous carbonates. It is also possible that a flake of basement rock was incorporated in limestone at that time. Indeed, organic-rich layers which are also sometimes rich in pyrite occur locally within the Cretaceous limestones. This potential source of low Eh fluid and redox variations was discussed by Banks et al. (1991) using Fe/Mn trends. Furthermore, methane observed in fluid inclusion (Appendix 5) is an extremely effective-reducing agent. It could have played an important role in the formation of redox sensitive elements (e.g., Burisch et al. 2017) (Fig. 11).

Fig. 10 Stability of mineralogical assemblage in the Triassic pelites of the PPV thrust hanging-wall, according to redox-condition modeling under 300 °C system

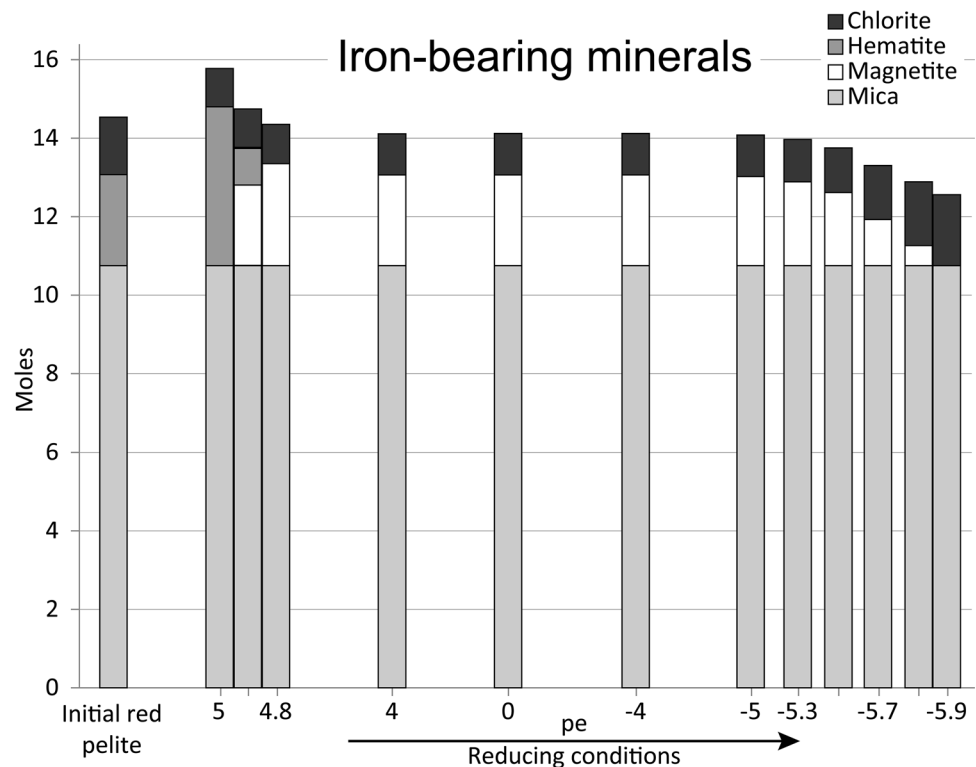
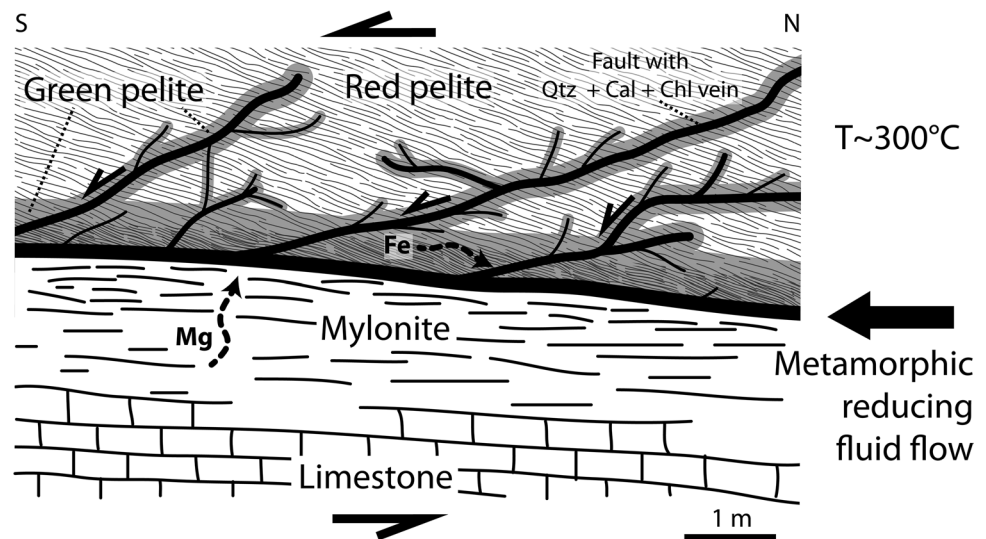


Fig. 11 Schematic model of fluid flow and mass transfers in the Pic-de-Port-Vieux thrust fault zone



The modeling results can be compared with several studies performed on thrust-related veins. Quartz fluid inclusions from syntectonic veins in the hanging-wall reveal two populations of hypersaline Sr-rich brine (Banks et al. 1991). The high Br/Cl ratio in these inclusions suggests an origin by evaporation of seawater with halite precipitation for the two populations (McCaig et al. 2000c). According to Banks et al. (1991) and McCaig et al. (1995, 2000c), the fluids trapped in the inclusions have the same origin (Ca/Na ratio similar), but their isotopic composition in Pb and Sr reflects the rock types in which they were stored. The brine could have derived from the upper Triassic evaporites and stored in the lower Triassic redbeds. Some of the formation water could have been stored in another host rock (whose nature has not been confirmed): in the Devonian basement or in the Silurian graphitic slates, for example (McCaig et al. 2000c). McCaig et al. (2000c) showed that in the quartz vein fluid inclusions, fluid was sucked into the PPV culmination from both footwall and hanging-wall. This fluid could have circulated through the Silurian graphitic schists. Indeed, the reductive fluid flow causing the hematite dissolution around flow channels might not be in equilibrium with redbeds. Carbonate veins show an isotopic composition similar to that of deformed carbonates and Silurian graphitic schists, thus indicating a fluid-flow regime different from that of the fluid inclusions in quartz (McCaig et al. 2000b). This suggests fluid interaction with deformed carbonates in the thrust footwall or Silurian graphitic schists before the precipitation in carbonate veins. Reduction of Na–Ca–Cl rich fluids is frequently observed, for example, causing uranium deposits in the Athabasca basin (Richard et al. 2015). According to the study of Bottrell and Yardley (1991), veins from sedimentary rocks which have undergone low-grade metamorphism show that the exchange between fluid and chlorite varies with the redox state of the wall rocks, while it is independent from the

salinity of the fluid. In summary, the very reducing fluid flow characterized along the PPV thrust was initially brine, i.e., an evaporitic formation water that was buffered with host rocks under greenschist facies metamorphism conditions. This brine was also called metamorphic water, because it has undergone metamorphic conditions (e.g., Lacroix and Vennemann 2015; Trincal et al. 2015).

Fluid-flow chronology and general considerations

Gavarnie–PPV thrust propagation

Grant et al. (1990) demonstrated that the PPV thrust corresponds to a Gavarnie thrust lower duplex branch and was accompanied by at least two stages of deformation. The structural investigation shows that both Gavarnie and PPV thrusts formed under the same stress field and likely correspond to a continuous deformation. The propagation of these two thrusts is associated with the footwall transformation, i.e., the replacement of Cretaceous dolomitic limestone by calc-mylonite. This transformation started in the early stage of Gavarnie thrust activity and could have continued until the end of the PPV culmination stage. Calc-mylonite formation is favored by an important fluid flow parallel to the thrust. This fluid, enriched in Sr isotope, was attributed to the upward migration of fluid from Triassic beds present at deeper levels than thrust (McCaig et al. 1995, 2000b, c). Calc-mylonite also recorded a $\delta^{18}\text{O}$ and $\delta^{13}\text{C}$ depletion and confirms this model. Indeed, the $\delta^{18}\text{O}$ composition of the fluid is $\sim 11\text{‰}$ and could be formed from a fluid in equilibrium with Triassic bed at 320 °C. However, due to the fabric anisotropy, this fluid flow was not sufficient enough to allow a large-scale isotopic front within the footwall. Yet, it is demonstrated that during this stage, the fluid-flow system

is assumed open with the contribution of km-scale derived fluid.

PPV culmination

The second stage of deformation, the PPV “culmination”, involves the formation of several duplex branches cutting footwall, hanging-wall, and mylonite (Grant, 1989). This stage is also contemporaneous with the formation of several sets of veins and fault within the PPV hanging-wall under low-grade metamorphic conditions (Trincal et al. 2015). In these conditions, hematite dissolution and chlorite formation in veins are related to iron mass transfers induced by a very reductive fluid. The temperatures estimated in chlorite and quartz veins are about 320 ± 50 °C. However, a greater range of temperatures was observed in the synkinematic veins and faults as revealed by quartz fluid inclusion studies (Grant 1990; Grant et al. 1990) and chlorite thermometry (Lacroix and Vennemann 2015; Trincal et al. 2015). Sr and Pb isotopes Banks et al. (1991) and Grant et al. (1990) showed the presence of hypersaline fluid (25 wt%) within vein fluid inclusions from PPV hanging-wall. According to these authors, this fluid could have derived from a local source within the hanging-wall. This was lately confirmed by McCaig et al. (2000c) based on Pb isotopic analysis. However, to obtain very anoxic conditions, fluid may have been reduced by interacting with methane as suggested by preliminary fluid inclusion Raman spectroscopy study (Appendix 5).

The PPV thrust juxtaposes pelites on dolomitic limestones. It allows the detailed investigation of fluid–rock interactions during deformation on two geochemically contrasted rocks under low-grade metamorphic conditions. Greenschist metamorphic facies is found at the interface between brittle and ductile domains, where mineralogical and geochemical behaviors remain poorly known during fluid-assisted deformation (e.g., Lacombe et al. 2014). Temperatures, mass transfer, and fluid-flow estimates performed in this study may be important for models of Pyrenean evolution, as well as for comparison with other similar fold-and-thrust belt sites (e.g., Glarus thrust, Morcle nappes, etc.).

Conclusion

The Pic-de-Port-Vieux thrust is a Pyrenean structure juxtaposing two geochemically contrasted rocks: the Triassic red pelite and the Cretaceous dolomitic limestone. The fault zone was chemically and mineralogically altered by an important synkinematic fluid flow. The processes responsible for this alteration were investigated by coupling detailed mineralogical and geochemical analyses on both pelite (hanging-wall) and carbonate (footwall).

In the footwall, mylonitization affects the dolomitic limestones up to 2 m from the thrust surface. Mylonitization occurred at about 300 °C and is related to plastic deformation. Indeed, calcite replaces dolomite and several carbonate generations have been characterized. The mineralogical transformations are due to fluid flow along the thrust. Regarding stable isotope composition of carbonate, the fluid might be an evaporite formation water buffered with Silurian rocks from the rock basement. Moreover, a Time-Integrated Fluid Flux (TIFF) perpendicular to calc-mylonites was estimated to $0.54 \text{ m}^3/\text{m}^2$, four magnitude orders lower than TIFF parallel to the thrust. We propose that this difference of fluid flux strongly depends to the fabric anisotropy, which is controlled by both strain and inherent tortuosity.

In the hanging-wall, pelite is affected by major fluid–rock interactions during thrusting. The dissolution of hematite and the gradual color transition from red to green pelites suggest the presence of an active reaction front during deformation, likely controlled by advective fluid from the mylonite to the pelites through the subsidiary faults. Hematite dissolution coupled with chlorite formation in veins suggests a very reductive fluid flow under low-grade metamorphic conditions (320 ± 50 °C).

Acknowledgements This work was partly supported by the French RENATECH network and its FEMTO-ST technological facility. Stable Isotope analysis were funded by the SNF-Swiss National Science Foundation project 20020-126973/1 to T. Vennemann. Authors wish to thank Andrew McCaig and Philippe Boulvais for their reviews that helped to considerably improve the discussion of this manuscript. Thanks to Olivier Fabbri for English corrections, Cyril Durand for fruitful discussions regarding isotopes and Eric Courgeon, guardian of Barroude refuge for his hospitality.

References

- Abart R, Badertscher N, Burkhard M, Povoden E (2002) Oxygen, carbon and strontium isotope systematics in two profiles across the Glarus thrust: implications for fluid flow. *Contrib Mineral Petr* 143:192–208
- Abd Elmola A, Charpentier D, Buatier M et al (2017) Textural-chemical changes and deformation conditions registered by phyllosilicates in a fault zone (Pic de Port Vieux thrust, Pyrenees). *Appl Clay Sci* 144:88–103
- Aja SU, Dyar DM (2002) The stability of Fe–Mg chlorites in hydrothermal solutions—I. Results of experimental investigations. *Appl Geochem* 17:1219–1239. doi:10.1016/S0883-2927(01)00131-7
- Aoya M, Kouketsu Y, Endo S et al (2010) Extending the applicability of the Raman carbonaceous-material geothermometer using data from contact metamorphic rocks. *J Metamorph Geol* 28:895–914. doi:10.1111/j.1525-1314.2010.00896.x
- Appelo CAJ, Postma D (2004) *Geochemistry, groundwater and pollution*. CRC Press, New York, p 648
- Badertscher NP, Abart R, Burkhard M, McCaig A (2002) Fluid flow pathways along the Glarus overthrust derived from stable and Sr-isotope patterns. *Am J Sci* 302:517–547
- Banks D, Davies G, Yardley BW et al (1991) The chemistry of brines from an Alpine thrust system in the Central Pyrenees:

- an application of fluid inclusion analysis to the study of fluid behaviour in orogenesis. *Geochim Cosmochim Acta* 55:1021–1030. doi:[10.1016/0016-7037\(91\)90160-7](https://doi.org/10.1016/0016-7037(91)90160-7)
- Baumgartner LP, Rumble D (1988) Transport of stable isotopes: I: development of a kinetic continuum theory for stable isotope transport. *Contrib Mineral Petr* 98:417–430
- Baumgartner LP, Valley JW (2001) Stable isotope transport and contact metamorphic fluid flow. *Rev Mineral Geochem* 43:415–467. doi:[10.2138/gsrng.43.1.415](https://doi.org/10.2138/gsrng.43.1.415)
- Beaudoin G, Therrien P (1999) Stable isotope fractionation calculator. In: AlphaDelta. http://www2.ggl.ulaval.ca/cgi-bin/alphadelta/alphadelta_4alpha.cgi/. Accessed 12 Jul 2016
- Bestmann M, Kunze K, Matthews A (2000) Evolution of a calcite marble shear zone complex on Thassos Island, Greece: microstructural and textural fabrics and their kinematic significance. *J Struct Geol* 22:1789–1807. doi:[10.1016/S0191-8141\(00\)00112-7](https://doi.org/10.1016/S0191-8141(00)00112-7)
- Beyssac O, Goffé B, Chopin C, Rouzaud JN (2002) Raman spectra of carbonaceous material in metasediments: a new geothermometer. *J Metamorph Geol* 20:859–871. doi:[10.1046/j.1525-1314.2002.00408.x](https://doi.org/10.1046/j.1525-1314.2002.00408.x)
- Bickle MJ, McKenzie D (1987) The transport of heat and matter by fluids during metamorphism. *Contrib Mineral Petrol* 95:384–392
- Bottrell SH, Yardley BWD (1991) The distribution of Fe and Mn between chlorite and fluid: evidence from fluid inclusions. *Geochim Cosmochim Acta* 55:241–244. doi:[10.1016/0016-7037\(91\)90414-Z](https://doi.org/10.1016/0016-7037(91)90414-Z)
- Bourdelle F, Benzerara K, Beyssac O et al (2013) Quantification of the ferric/ferrous iron ratio in silicates by scanning transmission X-ray microscopy at the Fe L_{2,3} edges. *Contrib Mineral Petrol* 166:423–434. doi:[10.1007/s00410-013-0883-4](https://doi.org/10.1007/s00410-013-0883-4)
- Bowen LH, Weed SB, Stevens JG (1969) Mossbauer study of micas and their potassium-depleted products. *Am Mineral* 54:72
- Bresser JD, Heege JT, Spiers C (2001) Grain size reduction by dynamic recrystallization: can it result in major rheological weakening? *Int J Earth Sci* 90:28–45. doi:[10.1007/s005310000149](https://doi.org/10.1007/s005310000149)
- Burisch M, Gerdes A, Walter BF et al (2017) Methane and the origin of five-element veins: mineralogy, age, fluid inclusion chemistry and ore forming processes in the Odenwald, SW Germany. *Ore Geol Rev* 81(Part 1):42–61. doi:[10.1016/j.oregeorev.2016.10.033](https://doi.org/10.1016/j.oregeorev.2016.10.033)
- Burkhard M (1990) Ductile deformation mechanisms in micritic limestones naturally deformed at low temperatures (150–350 °C). *Geol Soc Lond Spec Publ* 54:241–257
- Burkhard M, Kerrich R, Maas R, Fyfe WS (1992) Stable and Sr-isotope evidence for fluid advection during thrusting of the Glarus nappe (swiss alps). *Contrib Mineral Petrol* 112:293–311. doi:[10.1007/BF00310462](https://doi.org/10.1007/BF00310462)
- Busch JP, van der Pluijm BA (1995) Calcite textures, microstructures and rheological properties of marble mylonites in the Bancroft shear zone, Ontario, Canada. *J Struct Geol* 17:677–688. doi:[10.1016/0191-8141\(94\)00092-E](https://doi.org/10.1016/0191-8141(94)00092-E)
- Caine JS, Evans JP, Forster CB (1996) Fault zone architecture and permeability structure. *Geology* 24:1025–1028
- Cantarero I, Lanari P, Vidal O et al (2014) Long-term fluid circulation in extensional faults in the central Catalan Coastal Ranges: P–T constraints from neofomed chlorite and K-white mica. *Int J Earth Sci* 103:165–188
- Cathelineau M (1988) Cation site occupancy in chlorites and illites as a function of temperature. *Clay Miner* 23:471–485
- Charpentier D, Buatier MD, Jacquot E et al (2011) Conditions and mechanism for the formation of iron-rich Montmorillonite in deep sea sediments (Costa Rica margin): coupling high resolution mineralogical characterization and geochemical modeling. *Geochimica et Cosmochimica Acta* 75:1397–1410. doi:[10.1016/j.gca.2010.11.026](https://doi.org/10.1016/j.gca.2010.11.026)
- Cheary RW, Coelho A (1992) A fundamental parameters approach to X-ray line-profile fitting. *J Appl Crystallogr* 25:109–121. doi:[10.1107/S0021889891010804](https://doi.org/10.1107/S0021889891010804)
- Coe JMD (1980) Clay Miner and their transformations studied with nuclear techniques: the contribution of Mössbauer spectroscopy. *Atom Energy Rev* 18(1):73–124
- Cole DR, Ripley EM (1998) Oxygen isotope fractionation between chlorite and water from 170 to 350 °C: a preliminary assessment based on partial exchange and fluid/rock experiments. *Geochim Cosmochim Acta* 63:449–457
- De Grave E, Vandenbruwaene J, Bockstael MV (1987) 57Fe Mössbauer spectroscopic analysis of chlorite. *Phys Chem Mineral* 15:173–180. doi:[10.1007/BF00308781](https://doi.org/10.1007/BF00308781)
- Ebert A, Herwegh M, Pfiffner A (2007) Cooling induced strain localization in carbonate mylonites within a large-scale shear zone (Glarus thrust, Switzerland). *J Struct Geol* 29:1164–1184. doi:[10.1016/j.jsg.2007.03.007](https://doi.org/10.1016/j.jsg.2007.03.007)
- Faulkner DR, Jackson CAL, Lunn RJ et al (2010) A review of recent developments concerning the structure, mechanics and fluid flow properties of fault zones. *J Struct Geol* 32:1557–1575. doi:[10.1016/j.jsg.2010.06.009](https://doi.org/10.1016/j.jsg.2010.06.009)
- Ferrari AC, Robertson J (2000) Interpretation of Raman spectra of disordered and amorphous carbon. *Phys Rev B* 61:14095–14107. doi:[10.1103/PhysRevB.61.14095](https://doi.org/10.1103/PhysRevB.61.14095)
- Ferrill DA, Morris AP, Evans MA et al (2004) Calcite twin morphology: a low-temperature deformation geothermometer. *J Struct Geol* 26:1521–1529
- Ferry JM, Dipple GM (1991) Fluid flow, mineral reactions, and metasomatism. *Geology* 19:211–214
- Fisher QJ, Knipe RJ (2001) The permeability of faults within siliciclastic petroleum reservoirs of the North Sea and Norwegian Continental Shelf. *Mar Petrol Geol* 18:1063–1081
- Friedman I, O'Neil JR (1977) Data of geochemistry: Compilation of stable isotope fractionation factors of geochemical interest. US Government Printing Office
- Graham CM, Viglino JA, Harmon RS (1987) Experimental study of hydrogen-isotope exchange between aluminous chlorite and water and of hydrogen diffusion in chlorite. *Am Mineral* 72:566–579
- Grant NT (1989) Deformation and fluid processes in thrust sheets from the central Pyrenees. PhD University of London, p 320
- Grant NT (1990) Episodic discrete and distributed deformation: consequences and controls in a thrust culmination from the central Pyrenees. *J Struct Geol* 12:835–850. doi:[10.1016/0191-8141\(90\)90058-7](https://doi.org/10.1016/0191-8141(90)90058-7)
- Grant NT (1992) Post-emplacement extension within a thrust sheet from the central Pyrenees. *J Geol Soc Lond* 149:775–792. doi:[10.1144/gsjgs.149.5.0775](https://doi.org/10.1144/gsjgs.149.5.0775)
- Grant NT, Banks DA, McCaig AM, Yardley BWD (1990) Chemistry, source, and behavior of fluids involved in alpine thrusting of the central pyrenees. *J Geophys Res* 95:9123–9131. doi:[10.1029/JB095iB06p09123](https://doi.org/10.1029/JB095iB06p09123)
- Heller-Kallai L, Rozenson I (1981) The use of mössbauer spectroscopy of iron in clay mineralogy. *Phys Chem Mineral* 7:223–238. doi:[10.1007/BF00311893](https://doi.org/10.1007/BF00311893)
- Herwegh M, Berger A, Ebert A, Brodhag S (2008) Discrimination of annealed and dynamic fabrics: consequences for strain localization and deformation episodes of large-scale shear zones. *Earth Planet Sci Lett* 276:52–61
- Hudson JD (1977) Stable isotopes and limestone lithification. *J Geol Soc Lond* 133:637–660. doi:[10.1144/gsjgs.133.6.0637](https://doi.org/10.1144/gsjgs.133.6.0637)
- Jolivet M, Labaume P, Monié P et al (2007) Thermochronology constraints for the propagation sequence of the south Pyrenean basement thrust system (France–Spain). *Tectonics* 26:17. doi:[10.1029/2006TC002080](https://doi.org/10.1029/2006TC002080)

- Kasemann S, Meixner A, Rocholl A, Vennemann T, Rosner M, Schmitt AK, Wiedenbeck M (2001) Boron and oxygen isotope composition of certified reference materials NIST SRM 610/612 and reference materials JB-2 and JR-2. *Geostand Geoanalytical Res* 25(2–3):405–416
- Kim HM, Inoue J (2003) Analytical approach for anisotropic permeability through a single rough rock joint under shear deformation. *J Geophys Res Solid Earth* 108:2366
- Kirschner DL, Sharp ZD, Masson H (1995) Oxygen isotope thermometry of quartz-calcite veins: unraveling the thermal-tectonic history of the subgreenschist facies Morcles nappe (Swiss Alps). *Geol Soc Am Bull* 107:1145–1156. doi:[10.1130/0016-7606\(1995\)107<1145:OITOCQ>2.3.CO;2](https://doi.org/10.1130/0016-7606(1995)107<1145:OITOCQ>2.3.CO;2)
- Knipe RJ (1989) Deformation mechanisms—recognition from natural tectonites. *J Struct Geol* 11:127–146. doi:[10.1016/0191-8141\(89\)90039-4](https://doi.org/10.1016/0191-8141(89)90039-4)
- Knipe RJ, McCaig AM (1994) Microstructural and microchemical consequences of fluid flow in deforming rocks. *Geol Soc Lond Spec Publ* 78:99–111
- Kodama H, Longworth G, Townsend MG (1982) A Mössbauer investigation of some chlorites and their oxidation products. *Can Mineral* 20:585–592
- Labaume P, Meresse F, Jolivet M et al (2016) Tectonothermal history of an exhumed thrust-sheet-top basin: an example from the south Pyrenean thrust belt. *Tectonics* 35:1280–1313
- Lacombe O, Swennen R, Caracausi A (2014) Fluid–rock–tectonics interactions in basins and orogens. *Mar Petrol Geol* 55:1–5. doi:[10.1016/j.marpetgeo.2014.03.007](https://doi.org/10.1016/j.marpetgeo.2014.03.007)
- Lacroix B, Vennemann T (2015) Empirical calibration of the oxygen isotope fractionation between quartz and Fe–Mg-chlorite. *Geochim Cosmochim Acta* 149:21–31. doi:[10.1016/j.gca.2014.10.031](https://doi.org/10.1016/j.gca.2014.10.031)
- Lacroix B, Travé A, Buatier M et al (2014) Syntectonic fluid-flow along thrust faults: example of the South-Pyrenean fold-and-thrust belt. *Mar Petrol Geol* 49:84–98. doi:[10.1016/j.marpetgeo.2013.09.005](https://doi.org/10.1016/j.marpetgeo.2013.09.005)
- Lahfid A, Beyssac O, Deville E et al (2010) Evolution of the Raman spectrum of carbonaceous material in low-grade metasediments of the Glarus Alps (Switzerland). *Terr Nova* 22:354–360. doi:[10.1111/j.1365-3121.2010.00956.x](https://doi.org/10.1111/j.1365-3121.2010.00956.x)
- Lanari P (2012) Micro-cartographie P-T-ε dans les roches métamorphiques. PhD Université de Grenoble, Applications aux Alpes et à l'Himalaya, p 536p
- Lanari P, Guillot S, Schwartz S et al (2012) Diachronous evolution of the alpine continental subduction wedge: evidence from P–T estimates in the Briançonnais Zone houillère (France–Western Alps). *J Geodyn* 56–57:39–54. doi:[10.1016/j.jog.2011.09.006](https://doi.org/10.1016/j.jog.2011.09.006)
- Lanari P, Wagner T, Vidal O (2014) A thermodynamic model for di-trioctahedral chlorite from experimental and natural data in the system MgO–FeO–Al₂O₃–SiO₂–H₂O: applications to P–T sections and geothermometry. *Contrib Mineral Petrol* 167:1–19. doi:[10.1007/s00410-014-0968-8](https://doi.org/10.1007/s00410-014-0968-8)
- Longstaffe FJ (1987) Stable isotope studies of diagenetic processes. In: *Short course in stable isotope geochemistry of low temperature fluids*. Mineralogical Association of Canada Saskatoon, pp 187–257
- Matsuhisa Y, Goldsmith JR, Clayton RN (1979) Oxygen isotopic fractionation in the system quartz-albite-anorthite-water. *Geochim Cosmochim Acta* 43:1131–1140
- McCaig AM, Wayne DM, Marshall JD et al (1995) Isotopic and fluid inclusion studies of fluid movement along the Gavarnie Thrust, central Pyrenees; reaction fronts in carbonate mylonites. *Am J Sci* 295:309–343. doi:[10.2475/ajs.295.3.309](https://doi.org/10.2475/ajs.295.3.309)
- McCaig AM, Tritlla J, Banks D (2000a) Fluid flow patterns during Pyrenean thrusting. *J Geochem Explor* 69–70:539–543. doi:[10.1016/S0375-6742\(00\)00060-1](https://doi.org/10.1016/S0375-6742(00)00060-1)
- McCaig AM, Tritlla J, Banks D (2000b) Fluid mixing and recycling during Pyrenean thrusting: evidence from fluid inclusion halogen ratios. *Geochim Cosmochim Acta* 64:3395–3412. doi:[10.1016/S0016-7037\(00\)00437-3](https://doi.org/10.1016/S0016-7037(00)00437-3)
- McCaig AM, Wayne D, Rosenbaum J (2000c) Fluid expulsion and dilatancy pumping during thrusting in the Pyrenees: pb and Sr isotope evidence. *Geol Soc Am Bull* 112:1199–1208. doi:[10.1130/0016-7606\(2000\)112<1199:FEADPD>2.3.CO;2](https://doi.org/10.1130/0016-7606(2000)112<1199:FEADPD>2.3.CO;2)
- Merlet C, Bodinier J-L (1990) Electron microprobe determination of minor and trace transition elements in silicate minerals: a method and its application to mineral zoning in the peridotite nodule PHN 1611. *Chem Geol* 83:55–69
- Molli G, White JC, Kennedy L, Taini V (2011) Low-temperature deformation of limestone, Isola Palmaria, northern Apennine, Italy—The role of primary textures, precursory veins and intracrystalline deformation in localization. *J Struct Geol* 33:255–270. doi:[10.1016/j.jsg.2010.11.015](https://doi.org/10.1016/j.jsg.2010.11.015)
- Moore DM, Reynolds RC (1997) X-ray diffraction and the identification and analysis of Clay Miner. Oxford University Press, New York, p 322p
- Muñoz JA (1992) Evolution of a continental collision belt: ECORS-Pyrenees crustal balanced cross-section. In: McClay KR (ed) *Thrust tectonics*. Springer, Dordrecht, pp 235–246
- Nelson CS, Smith AM (1996) Stable oxygen and carbon isotope compositional fields for skeletal and diagenetic components in New Zealand Cenozoic nontropical carbonate sediments and limestones: a synthesis and review
- Nesbitt BE, Muehlenbachs K (1995) Geochemical studies of the origins and effects of synorogenic crustal fluids in the southern Omineca Belt of British Columbia, Canada. *Geol Soc Am Bull* 107:1033–1050. doi:[10.1130/0016-7606\(1995\)107<1033:GSO TOA>2.3.CO;2](https://doi.org/10.1130/0016-7606(1995)107<1033:GSO TOA>2.3.CO;2)
- O'Neil JR, Clayton RN, Mayeda TK (1969) Oxygen isotope fractionation in divalent metal carbonates. Univ. of Chicago
- Parish M (1984) A structural interpretation of a section of the Gavarnie nappe and its implications for Pyrenean geology. *J Struct Geol* 6:247–255. doi:[10.1016/0191-8141\(84\)90049-X](https://doi.org/10.1016/0191-8141(84)90049-X)
- Parkhurst DL (1995) User's guide to PHREEQC: A computer program for speciation, reaction-path, advective-transport, and inverse geochemical calculations
- Parkhurst DL, Appelo CAJ (1999) User's guide to PHREEQC (Version 2): a computer program for speciation, batch-reaction, one-dimensional transport, and inverse geochemical calculations
- Pasteris J-D, Wopenka B (1991) Raman spectra of graphite as indicators of degree of metamorphism. *Can Mineral* 29:1–9
- Pfiffner OA (1982) Deformation mechanisms and flow regimes in limestones from the Helvetic zone of the Swiss Alps. *J Struct Geol* 4:429–442. doi:[10.1016/0191-8141\(82\)90034-7](https://doi.org/10.1016/0191-8141(82)90034-7)
- Pfiffner OA (1985) Displacements along thrust faults. *Eclogae Geol Helv* 78:313–333
- Prokoph A, Shields GA, Veizer J (2008) Compilation and time-series analysis of a marine carbonate δ¹⁸O, δ¹³C, 87Sr/86Sr and δ³⁴S database through Earth history. *Earth Sci Rev* 87:113–133. doi:[10.1016/j.earscirev.2007.12.003](https://doi.org/10.1016/j.earscirev.2007.12.003)
- Rancourt DG, Ping JY (1991) Voigt-based methods for arbitrary-shape static hyperfine parameter distributions in Mössbauer spectroscopy. *Nucl Instrum Methods B* 58:85–97. doi:[10.1016/0168-583X\(91\)95681-3](https://doi.org/10.1016/0168-583X(91)95681-3)
- Richard A, Cathelineau M, Boiron M-C et al (2015) Metal-rich fluid inclusions provide new insights into unconformity-related U deposits (Athabasca Basin and Basement, Canada). *Miner Deposit* 51:249–270. doi:[10.1007/s00126-015-0601-4](https://doi.org/10.1007/s00126-015-0601-4)
- Rietveld HM (1969) A profile refinement method for nuclear and magnetic structures. *J Appl Crystallogr* 2:65–71. doi:[10.1107/S0021889869006558](https://doi.org/10.1107/S0021889869006558)

- Roure F, Choukroune P, Berastegui X et al (1989) Ecors deep seismic data and balanced cross sections: geometric constraints on the evolution of the Pyrenees. *Tectonics* 8:41–50. doi:[10.1029/TC008i001p00041](https://doi.org/10.1029/TC008i001p00041)
- Rumble D, Hoering TC (1994) Analysis for oxygen and sulfur isotope ratios in oxide and sulfide minerals by spot heating with a carbon dioxide laser in a fluorine atmosphere. *Acc Chem Res* 27:237–241
- Rye DM, Bradbury HJ (1988) Fluid flow in the crust; an example from a Pyrenean thrust ramp. *Am J Sci* 288:197–235. doi:[10.2475/ajs.288.3.197](https://doi.org/10.2475/ajs.288.3.197)
- Savin SM, Lee ML (1988) Isotopic studies of phyllosilicates. *Rev Mineral Geochem* 19:189–223
- Schenk O, Urai JL, Evans B (2005) The effect of water on recrystallization behavior and grain boundary morphology in calcite—observations of natural marble mylonites. *J Struct Geol* 27:1856–1872. doi:[10.1016/j.jsg.2005.05.015](https://doi.org/10.1016/j.jsg.2005.05.015)
- Sharp ZD (2009) Application of stable isotope geochemistry to low-grade metamorphic rocks. *Low-Grade Metamorphism* 227–260
- Soler D, Teixell A, García-Sansegundo J (1998) Amortissement latéral du chevauchement de Gavarnie et sa relation avec les unités sud-pyrénéennes. *CR Acad Sci II A* 327:699–704. doi:[10.1016/S1251-8050\(99\)80028-7](https://doi.org/10.1016/S1251-8050(99)80028-7)
- Spötl C, Vennemann TW (2003) Continuous-flow isotope ratio mass spectrometric analysis of carbonate minerals. *Rapid Commun Mass Spectrom* 17:1004–1006
- Tarantola A, Mullis J, Guillaume D et al (2009) Oxidation of CH₄ to CO₂ and H₂O by chloritization of detrital biotite at 270 ± 5 °C in the external part of the Central Alps, Switzerland. *Lithos* 112:497–510. doi:[10.1016/j.lithos.2009.04.008](https://doi.org/10.1016/j.lithos.2009.04.008)
- Taylor JC, Hinczak I (2003) Rietveld made easy: a practical guide to the understanding of the method and successful phase quantifications. Sietronics Pty Ltd., Canberra, p 201p
- Teixell A (1998) Crustal structure and orogenic material budget in the west central Pyrenees. *Tectonics* 17:395–406. doi:[10.1029/98TC00561](https://doi.org/10.1029/98TC00561)
- Teixell A (2000) Geotectónica de los Pirineos. *Investigación y Ciencia* 288:54–65
- Trincal V, Lanari P (2016) Al-free di-trioctahedral substitution and a ferri-sudoite end-member evidenced in chlorite. *Clays Miner* 51:675–689. doi:[10.1180/claymin.2016.051.4.09](https://doi.org/10.1180/claymin.2016.051.4.09)
- Trincal V, Charpentier D, Buatier MD et al (2014) Quantification of mass transfers and mineralogical transformations in a thrust fault (Monte Perdido thrust unit, southern Pyrenees, Spain). *Mar Petrol Geol* 55:160–175. doi:[10.1016/j.marpetgeo.2013.12.016](https://doi.org/10.1016/j.marpetgeo.2013.12.016)
- Trincal V, Lanari P, Buatier M et al (2015) Temperature micro-mapping in oscillatory-zoned chlorite: application to study of a greenschist facies fault zone in the Pyrenean Axial Zone (Spain). *Am Mineral* 100:2468–2483. doi:[10.2138/am-2015-5217](https://doi.org/10.2138/am-2015-5217)
- Van der Pluijm B (1991) Marble mylonites in the Bancroft shear zone, Ontario, Canada: microstructures and deformation mechanisms. *J Struct Geol* 13:1125–1135
- Veizer J, Ala D, Azmy K et al (1999) 87Sr/86Sr, $\delta^{13}\text{C}$ and $\delta^{18}\text{O}$ evolution of Phanerozoic seawater. *Chem Geol* 161:59–88. doi:[10.1016/S0009-2541\(99\)00081-9](https://doi.org/10.1016/S0009-2541(99)00081-9)
- Vidal O, Parra T, Vieillard P (2005) Thermodynamic properties of the Tschermak solid solution in Fe-chlorite: application to natural examples and possible role of oxidation. *Am Mineral* 90:347–358. doi:[10.2138/am.2005.1554](https://doi.org/10.2138/am.2005.1554)
- Vidal O, De Andrade V, Lewin E et al (2006) P–T-deformation-Fe³⁺/Fe²⁺ mapping at the thin section scale and comparison with XANES mapping: application to a garnet-bearing metapelite from the Sambagawa metamorphic belt (Japan). *J Metamorph Geol* 24:669–683. doi:[10.1111/j.1525-1314.2006.00661.x](https://doi.org/10.1111/j.1525-1314.2006.00661.x)
- Vidal O, Lanari P, Munoz M et al (2016) Temperature, pressure, oxygen activity conditions of chlorite formation. *Clay Miner* 51(4):615–633
- Wigley M, Kampman N, Dubacq B, Bickle M (2012) Fluid–mineral reactions and trace metal mobilization in an exhumed natural CO₂ reservoir, Green River, Utah. *Geology* 40:555–558. doi:[10.1130/G32946.1](https://doi.org/10.1130/G32946.1)
- Wigley M, Dubacq B, Kampman N, Bickle M (2013) Controls of sluggish, CO₂-promoted, hematite and K-feldspar dissolution kinetics in sandstones. *Earth Planet Sci Lett* 362:76–87. doi:[10.1016/j.epsl.2012.11.045](https://doi.org/10.1016/j.epsl.2012.11.045)
- Zhang S, Cox SF (2000) Enhancement of fluid permeability during shear deformation of a synthetic mud. *J Struct Geol* 22:1385–1393
- Zhang S, Tullis TE (1998) The effect of fault slip on permeability and permeability anisotropy in quartz gouge. *Tectonophysics* 295:41–52
- Zhang Y, Underschultz JR, Gartrell A et al (2011) Effects of regional fluid pressure gradients on strain localisation and fluid flow during extensional fault reactivation. *Mar Petrol Geol* 28:1703–1713. doi:[10.1016/j.marpetgeo.2011.07.006](https://doi.org/10.1016/j.marpetgeo.2011.07.006)
- Zheng Y-F (1999) Oxygen isotope fractionation in carbonate and sulfate minerals. *Geochem J* 33:109–126